

The interacting pair of galaxies Arp 82: Integral field spectroscopy and numerical simulations

Prime Karera,^{1,2}  Laurent Drissen,^{1,2} Hugo Martel,^{1,2} Jorge Iglesias-Páramo,³ Jose M. Vilchez,³ Pierre-Alain Duc,⁴ and Henri Plana⁵

¹Département de Physique, de génie physique et d'optique, Université Laval, Québec (QC), G1V 0A6, Canada

²Centre de recherche en astrophysique du Québec, Québec (QC), Canada

³Instituto de Astrofísica de Andalucía (CSIC), Glorieta de la Astronomía s/n, Aptdo. 3004, 18080 Granada, Spain

⁴Observatoire Astronomique de Strasbourg (ObAS) 11, rue de l'Université, F-67000 Strasbourg, France

⁵Laboratório de Astrofísica Teórica e Observacional, Universidade Estadual de Santa Cruz, 45650-000 Ilhéus, BA, Brasil

Accepted 2022 May 23. Received 2022 May 22; in original form 2022 February 14

ABSTRACT

Spectral data cubes of the interacting pair of galaxies NGC 2535 and NGC 2536 (the Arp 82 system) targeting bright emission lines in the visible band, obtained with the imaging Fourier transform spectrometer (iFTS) SITELE attached to the Canada-France-Hawaii Telescope (CFHT), are presented. Analysis of H α velocity maps reveals a bar in NGC 2536. In NGC 2535, we find strong non-circular motions outside the ocular ring, in the elliptical arc and tidal tails of NGC 2535 and a misalignment between the kinematic and photometric position angles. We detect 155 HII region complexes in the interacting pair of galaxies and determine oxygen abundances for 66 of them using different calibrators. We find, regardless of the indicator used, that the oxygen abundance distribution in NGC 2536 is shallow whereas, in NGC 2535, it is best fitted by two slopes, the break occurring beyond the ocular ring. The inner slope is comparable to the one observed in isolated normal star-forming galaxies but the outer slope is shallow. We present a numerical simulation of the interaction that reproduces the observed tidal features, kinematics, and metallicity distribution, to investigate the effect of the interaction on the galaxies. The model indicates that the galaxies have undergone a close encounter, strongly prograde for the primary, and are half way in their course to a second close encounter.

Key words: galaxies :individual (Arp 82, NGC 2535, NGC 2536) – galaxies :interactions – galaxies :abundances – galaxies :kinematics and dynamics – methods :numerical

1 INTRODUCTION

Galaxy interactions are fundamental in the evolution of the Universe. Early numerical simulations (Toomre & Toomre 1972; Toomre 1977) demonstrated that gravitational forces between merging or interacting galaxies were responsible for the distorted morphologies observed in these peculiar systems. Later, simulations taking into account the hydrodynamics of the gaseous component (e.g., Mihos & Hernquist 1994; Di Matteo et al. 2007; Blumenthal & Barnes 2018), suggested that tidal forces may funnel gas to the central regions and fuel massive star formation (SF) and/or active galactic nuclei (AGN). These theoretical predictions are supported by observational studies (Ellison et al. 2013, and references therein). Specifically, ultraluminous infrared galaxies (ULIRGs) at low redshifts, i.e. the strongest starbursts in the local Universe, are found preferentially in merging and interacting galaxies (Sanders & Mirabel 1996; Knapen et al. 2015). The inflow of metal-poor gas towards the centre of the galaxy dilutes the nuclear metallicity and flattens the initial metallicity gradient as has been observed in some nearby galaxy pairs (Kewley

et al. 2006, 2010) and reproduced by numerical simulations (Rupke et al. 2010).

However, induced SF is not always localized in interacting galaxies. It can be spatially extended (Renaud et al. 2015) and, under favorable conditions, gravitationally bound tidal dwarf galaxies (TDGs) can form up to the tip of tidal tails (Duc 2012). The magnitude of induced changes strongly depend on the interaction stage, orbital parameters and intrinsic properties of the colliding galaxies. For instance, distant passages (usually at an early stage of interaction) trigger an increase in the SF activity over large volumes, whereas, closer, penetrating encounters (usually at later stages before coalescence) increase nuclear activity. Moreover, Barrera-Ballesteros et al. (2015) report central oxygen abundances in a sample of interacting galaxies similar to those in a control sample, suggesting that other processes such as stellar feedback contribute to lower central metallicity depression in interacting galaxies. Therefore, to understand galaxy-galaxy interactions, a combination of 2D spectroscopic and imaging data, which yields simultaneous information on morphology, SF, metallicity, etc. is needed. Comparison of observations to numerical models of the interactions can provide information about orbital parameters, timescales and SF triggering mechanisms (Renaud et al. 2015). At a minimum, a numerical model should repro-

*. E-mail: prime.karera.1@ulaval.ca (KTS)

duce the morphology and kinematics of the system (Privon et al. 2013). Insights on metallicity distribution would further constrain the numerical model. To compare the velocity fields of simulations and observations, we need to have relatively high velocity resolution and spatial resolution for the systems being modelled. There are only a few systems where these kinematic data with high resolutions and spatially covering both the parents disk galaxies, the tidal features and possible TDGs are available (Bournaud et al. 2004).

In this article, we are aiming to investigate the impact of interactions on the properties of the ionized gas in the pair of galaxies Arp 82, an M51-like double system that consists of NGC 2535, a galaxy with grand-design spiral arms and a companion, NGC 2536, at the end of one of the tidal tails. NGC 2535 has an eye-shaped structure connecting the two tidal arms reminiscent of the ocular galaxy IC 2163. 2D velocity maps were obtained by Amram et al. (1989) in H α and by Kaufman et al. (1997) in HI line. 1D velocity and metallicity measurements were also obtained by Zasov et al. (2019) using two long slits, one connecting the centres of the galaxies and the other running along the bridge and crossing NGC 2536. Using broadband UV and optical colors, combined to population synthesis models, Hancock et al. (2007) find that the stellar population is essentially of young to intermediate ages. Numerical models that successfully reproduce the morphology of the system (Howard et al. 1993; Kaufman et al. 1997; Hancock et al. 2007; Holincheck et al. 2016) agree on the fact that the interaction is strongly prograde for the primary galaxy but differ, for example, in mass ratios and time elapsed since closest approach.

In this work, we study the ionized gas properties of Arp 82 using SITELLE data cubes and present a numerical SPH model of the interacting galaxies. We adopt a distance of 59.2 Mpc from Zaragoza-Cardiel et al. (2018); at this distance, $1'' \sim 285$ pc. With its large field of view ($11' \times 11'$) and flexible spectral resolution up to $R = 10000$ in filter-selected regions of the visible range, the CFHT imaging Fourier transform spectrometer (iFITS) SITELLE (Drissen et al. 2014, 2019) is very well-suited to tackle this problem; its spatial resolution is seeing-limited and sampled at $0.32''$ per pixel. At the distance of Arp 82, the instrument allows a spatial resolution of 215 pc ($0.75''$ seeing) up to ~ 188 kpc from the central galaxies. We derive rotation curves, surface brightness, and oxygen abundance profiles for both galaxies and discuss the evolution of the SF activity and metallicity during the interaction.

This paper is organised as follows. In Section 2 we describe our observations, data reduction and calibration. In Section 3 we describe our data analysis. We present our numerical model in Section 4. Finally, we summarize our results in Section 5.

2 OBSERVATIONS, DATA REDUCTION AND CALIBRATION

Arp 82 was observed with SITELLE in November 2016 in three spectral bands allowing measurements of the strong emission lines : SN1 filter for [OII] $\lambda\lambda 3727, 3729$, SN2 filter for H β and [OIII] $\lambda\lambda 4959, 5007$, and SN3 filter for H α , [NII] $\lambda\lambda 6548, 6583$ and [SII] $\lambda\lambda 6716, 6731$. Details and technical specifications of the observations are listed in Table 1. Fig. 1 shows a combination of the deep images for the SN2 and SN3 cubes; these images are produced by summing all interferograms obtained by the instrument before performing the Fourier transform. Features such as the bright eye-shaped structure in NGC 2535 and the extended tidal arms are easily seen.

Data reduction was performed using ORBS and ORCS (Martin et al. 2015), SITELLE's dedicated data reduction and analysis pipe-



FIGURE 1. Composite colored image of Arp 82 obtained with SITELLE (blue : SN2 deep image, red : SN3 deep image, green : mean of SN2 and SN3 deep images). North is up and East is left. The image spans $4.9' \times 4.6'$.

TABLE 1. Observation Log.

Filter	Band [Å]	Spectral resolution	Exp. time per step [sec]	# of steps
SN1	3650 - 3850	960	39	172
SN2	4800 - 5800	970	40	225
SN3	6510 - 6850	1900	25	337

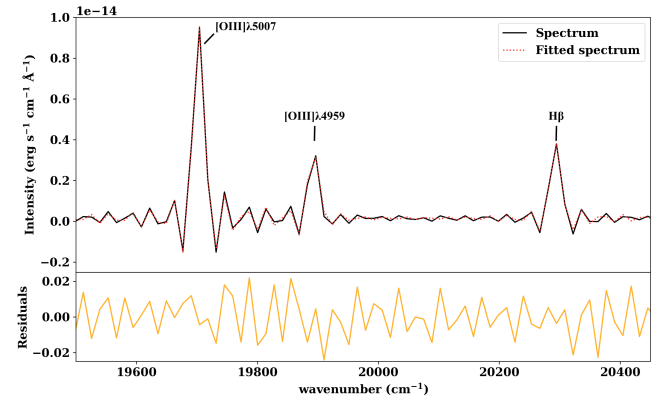


FIGURE 2. Example of a fit of the spectrum of a bright star-forming region in NGC 2535. The good quality of the fit of emission lines by sinc-shaped profiles is evidenced by the very small residuals.

lines. Details of the automated procedure as well as the sources of uncertainties can be found in Martin et al. (2021). The wavelength calibration is performed using a high resolution laser source but may show distortions (up to 25 km/s across the field of view) due to aberrations and deformations in the optical structure (Martin et al. 2016). To refine the wavelength calibration, we measured the centroid positions of the night sky OH emission lines (in the SN3 filter) in spectra extracted from circular regions sampling the entire FOV, following

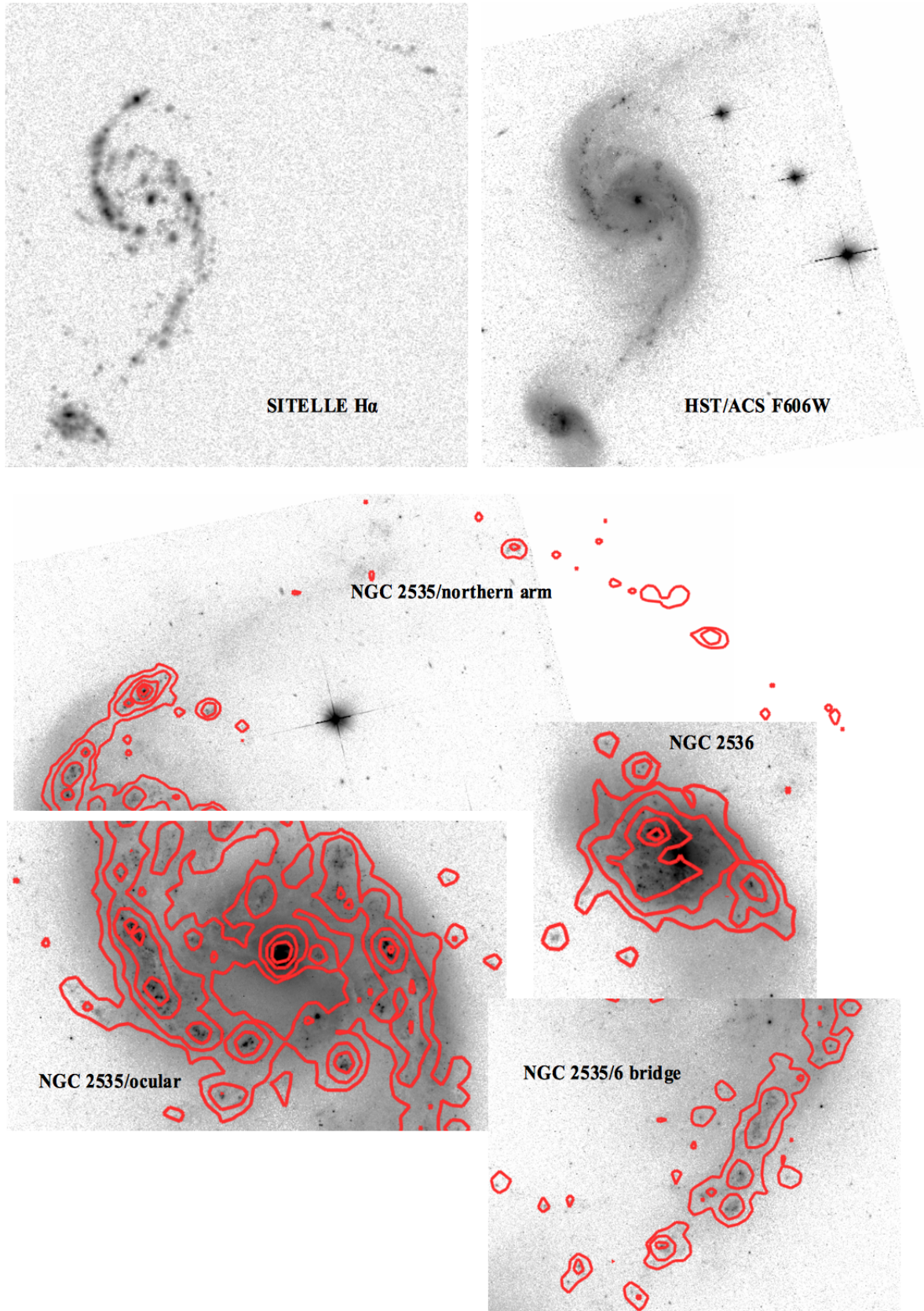


FIGURE 3. Expanded view of H α flux map at SITELLE full resolution (top left) and archival HST ACS/F606W image (top right). Zoom in view of the HST image with SITELLE H α contours overplotted (mosaic in lower panels) : there is a correlation of H α emission to the presence of ionizing young stellar sources. H α contour levels are $[5, 16, 63, 239, 504] \times 10^{-18} \text{ erg s}^{-1} \text{ cm}^{-2}$.

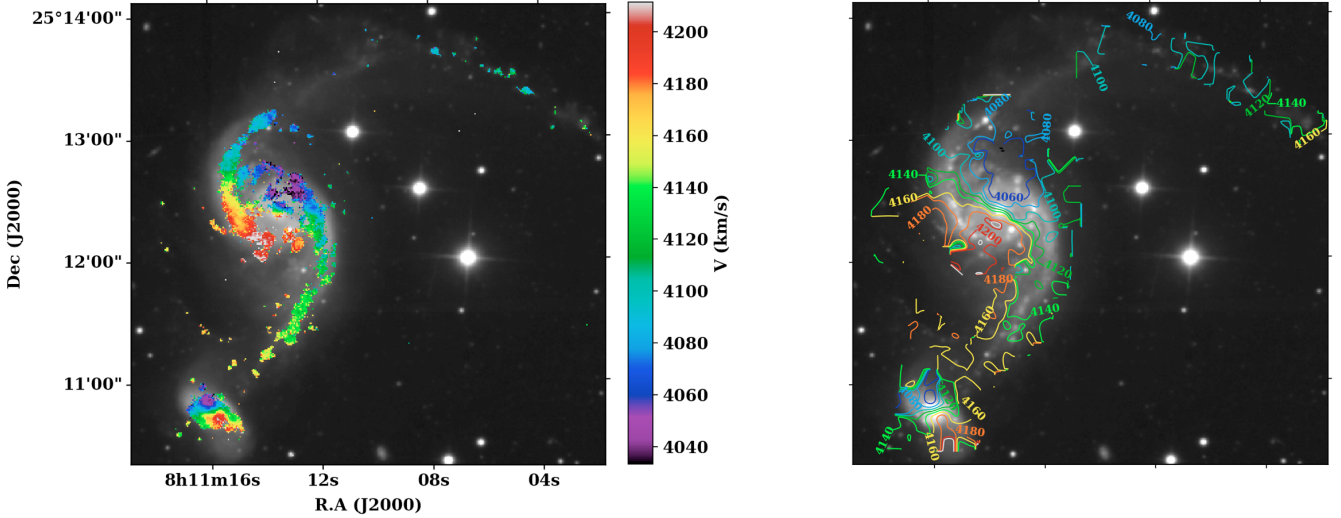


FIGURE 4. $H\alpha$ velocity map (left) and corresponding isovelocity contours (right) superimposed on the SN3 deep image. The corresponding map of velocity uncertainty is shown in Fig. A1. Contours were generated from the velocity maps smoothed with a gaussian 2D kernel of 2.5 pixels.

the procedure described in [Martin et al. \(2018\)](#). A velocity correction map is obtained by interpolating values on the night sky velocity grid, reducing the uncertainty on the velocity calibration across the entire field to less than 2 km/s. We also applied a barycentric correction of +24.71 km/s. Photometric calibration was performed using images and datacubes of spectrophotometric standard stars.

Given that the spatial resolution is seeing-limited ($\sim 0.75''$), the spaxels have been binned 2×2 during the line extraction process to increase the signal-to-noise ratio (SNR) of faint regions. Emission lines are fitted for each spaxel after subtracting a median sky spectrum taken in a dark circular region (aperture of $13''$) far away from the galaxies. Line fitting for SN1 and SN2 data cubes are done using sinc-shaped profiles, the natural instrument line shape of iFITS, as illustrated in Fig. 2. The higher spectral resolution and SNR achieved for the SN3 data cube allows us to fit these lines using a sincgauss function (a sinc function convolved with a gaussian; see [Martin et al. \(2016\)](#) for details) and thus map the velocity dispersion of the ionized gas. The software produces maps of fluxes of fitted emission lines, continuum level, velocity, and velocity dispersion (the last three parameters are common to all lines in one data cube) together with maps of their corresponding uncertainties. While the SN1 and SN2 cubes were obtained under photometric conditions, it was not the case for the SN3 cube. We therefore compared our $H\alpha$ + $[NII]$ fluxes with those obtained by [Kennicutt et al. \(1987\)](#). SN3 flux maps ($H\alpha$, $[NII]\lambda\lambda 6548, 6583$, $[SII]\lambda\lambda 6716, 6731$) are thereafter corrected to match [Kennicutt et al. \(1987\)](#) data. Flux maps of extracted emission lines and the velocity dispersion map from the SN3 cube are presented in Fig. A1. For illustration, we show in Fig. 3 (top left) the $H\alpha$ flux map at full resolution. Several bright HII region complexes can be identified in both galaxies, the faintest regions being located in the tidal tails far from the galaxies centres. This $H\alpha$ emission results from young stellar sources ionizing their surrounding interstellar medium. The correlation can be seen in the zoom in snapshots of Fig. 3 where peaks of $H\alpha$ emission coincides with loci of bright star-forming knots visible in the sharp archival Hubble Space Telescope (HST) Advanced Camera for Surveys (ACS) image (filter F606W). Star forming regions, as revealed in SITELLE and HST images of Fig. 3, are not only confined in the centres of the galaxies. Both

images reveal that star formation rate (SFR) is greater in the ocular and spiral structures and lower in the tidal tails (as shall be quantified in Section 3 from $H\alpha$ fluxes corrected for extinction), although the northern tail of NGC 2535 is truncated in the HST image. We also note that the $H\alpha$ flux in the central region of NGC 2536 (including the bar) is relatively weak, the brightest HII region complexes being clearly offset from the core of the galaxy. The analysis in the following section is based on the spectral properties of the ionized gas in the interacting system.

3 DATA ANALYSIS

3.1 Kinematics and surface brightness

The line-of-sight velocity maps obtained from fitting SN3 emission lines of the ionized gas are presented in Fig. 4. Only data points with $H\alpha$ fluxes $> 2 \times 10^{-17} \text{ erg s}^{-1} \text{ cm}^{-2}$, $\text{SNR} > 3$ and measured velocity uncertainties $< 20 \text{ km s}^{-1}$ were used. The isovelocity contours, although very distorted, show an overall "spider" pattern characteristic of differentially rotating inclined disks. For both galaxies, approaching/receding sides have projected velocities lesser/greater than 4100/4140 km s^{-1} , with systemic velocities $\sim 4120 \text{ km s}^{-1}$. The line of nodes in NGC 2535 lies in the direction joining the centres of the two galaxies; in NGC 2536 it lies in the direction joining the tips of the spiral arms. Assuming that both galaxies have trailing arms, they both rotate counterclockwise.

The velocity fields of the galaxies are very perturbed. Isovelocity contours tend to run parallel to spiral arms with velocity kinks indicative of peculiar velocities or streaming motions. The velocity kinks are also observed in the HI velocity map of [Kaufman et al. \(1997\)](#) in which an elliptical arc is identified with a position angle (P.A.) of 172° . This feature coincides in our velocity map to the loci of velocity kinks around NGC 2535 delimited to the south-east by the curved spur of HII regions right above NGC 2536 and to the north-west by the string of HII regions intersecting the tidal arm at $\sim [8h11m14s, 25^\circ 13'00'']$. The ellipse is off-centered as isovelocity contours are more elongated on the receding side. The ocular ring and the smaller spurs that appear attached to the ring at its southern

rim and the one right above the ring's northern rim are not seen in the HI map as the central part of NGC 2535 is located in an HI trough filled in with ^{12}CO emission (Kaufman et al. 1997). The link between these features and the ongoing interaction between the two galaxies is discussed in Section 4.

We extract kinematic parameters of the interacting galaxies by modelling their velocity fields with DiskFit (Spekkens & Sellwood 2007; Sellwood & Sánchez 2010; Sellwood & Spekkens 2015). The code can fit axisymmetric and non-axisymmetric motions in two-dimensional velocity fields, as well as perform fits of outer disk symmetric warps. A model is fitted to regularly spaced, concentric ellipses at radii specified by the user, from which the kinematic parameters are derived assuming that the disk is flat (constant inclination and constant PA) and that the perturbation that drives the non-circular motions has a fixed principal axis. In our case, the separation between the ellipses were chosen to be two pixels to ensure that each ring contained a minimum of ten measured velocities at the lowest radii. The velocity model is given by the following expression :

$$V_{\text{model}} = V_{\text{sys}} + \sin i [\bar{V}_t \cos \theta - V_{m,t} \cos(m\theta_b) \cos \theta - V_{m,r} \sin(m\theta_b) \sin \theta] \quad (1)$$

where V_{sys} is the systemic velocity, \bar{V}_t is the circular velocity, $V_{m,t}$ and $V_{m,r}$ are the tangential and radial components of non-circular flows with harmonic order $m = 1$ or $m = 2$ in the disc plane, θ and θ_b are the azimuthal angles relative to the major axis and the non-circular flow axis, respectively, and i is the disk inclination. If $m = 1$, the model describes a lopsided flow; if $m = 2$ the model is bi-symmetric, and describes a barred or elliptical flow. For an axisymmetric model, $V_{m,t}$ and $V_{m,r}$ are set to zero.

To avoid strong deviations from pure circular motions in our data, we only fit the inner parts of the discs of the two galaxies. For example, sampling data points on the velocity map at position $\sim [8\text{h}11\text{m}12\text{s}, 25^\circ 13'00'']$ would induce a gradient in projected velocities of $\sim 60\text{ km/s}$ just across the northern spur of NGC 2535. A steep decrease in velocities would also occur for data points at approximately the same radius crossing the bridge. This behavior can be seen in the velocity profile of Amram et al. (1989). Also, velocities along the tidal tails (extended arm and bridge) seem to remain constant over long patches, in agreement with the long-slit spectral observations of Zasov et al. (2019). Results of the modelling are shown in Fig. 5. NGC 2535 is best fitted by an axisymmetric model (Fig. 5a). The residuals (Fig. 5e) of the rotation-only model (Fig. 5b) applied to NGC 2536 show clear indications of the presence of a non-axisymmetric flow. Adding a bar-like feature (Fig. 5c) to the rotation-only model significantly lowers the residuals (Fig. 5f). The choice of these models is also consistent with the structural components found in photometry modelling as discussed below. The best-fitting kinematic parameters are listed in Table 2. Uncertainties on the models parameters were estimated by generating 100 bootstrap realizations of each velocity model (Sellwood & Sánchez 2010). The derived systemic velocities of the two galaxies are very close. Their centres have a projected separation of $102''$ or 29 kpc for the adopted distance which transcribes to a deprojected separation of 30.5 kpc if NGC 2536 is in the plane of NGC 2535 disk. Fig. 5g and Fig. 5h show the radial velocity distribution of the best models. The projected velocity profiles of the models are in good agreement with those of Amram et al. (1989). A velocity profile extending beyond the ocular ring in NGC 2535, using the same kinematic parameters derived here, is presented in Section 4 and compared to the radial velocity distribution of the primary galaxy in the simulation. The decline in the velocity profile of NGC 2536 occurs at the position of

TABLE 2. Best-fitting kinematic parameters. x_c and y_c are positions of the kinematic centre, $\Phi_{\text{kin},d}$ is the PA of the kinematic major axis of the disk in the sky plane, $\Phi_{\text{kin},b}$ is the PA of the major axis of the bar in the disk plane. For velocity fields, PAs correspond to the receding side of the disk. V_a , r_t and c are parameters describing fits to the rotation curves (see Eq.(2)).

	NGC 2535	NGC 2536
x_c	8h11m13.5s	8h11m15.9s
y_c	+25°12'24.6''	+25°10'46.7''
$V_{\text{sys}} [\text{km s}^{-1}]$	4124.7 ± 1.4	4118.8 ± 1.2
i	$18.1^\circ \pm 9.9^\circ$	$48.1^\circ \pm 4.9^\circ$
$\Phi_{\text{kin},d}$	$154.1^\circ \pm 3.0^\circ$	$211.8^\circ \pm 4.5^\circ$
$\Phi_{\text{kin},b}$...	$56.0^\circ \pm 9.8^\circ$ ^a
$V_a [\text{km s}^{-1}]$	376.1 ± 44.2	155.3 ± 41.7
$r_t [\text{arcsec}]$	2.26 ± 0.56	1.88 ± 0.92
$c [\text{km s}^{-1} \text{ arcsec}^{-1}]$	-4.1 ± 1.9	-5.3 ± 2.6

^a DiskFit computes $\Phi_{\text{kin},b}$ in the disk plane so that Eq.(1) can apply. The corresponding value in the sky plane is 256.6° (see Eq.(6) of Spekkens & Sellwood (2007) for conversion details)

TABLE 3. Best-fitting photometric parameters. x_c and y_c are positions of the image centre, $\Phi_{\text{phot},d}$ is the PA of the major axis of the disk in the sky plane, $\Phi'_{\text{phot},b}$ is the PA of the major axis of the bar in the sky plane. $\epsilon_{\text{bar/bulge}}$ are apparent ellipticities of the bar/bulge components. $I_{e,\text{disk/bulge}}$, $r_{e,\text{disk/bulge}}$ and $n_{\text{disk/bulge}}$ are parameters describing fits to the disk/bulge brightness profiles (see eq.(3)). I_e brightness are in units of $10^{-17} \text{ erg s}^{-1} \text{ cm}^{-2} \text{ \AA}^{-1} \text{ arcsec}^{-2}$. The bottom three parameters are the percentages of light coming from the galaxy components.

	NGC 2535	NGC 2536
x_c	8h11m13.5s	8h11m15.9s
y_c	+25°12'24.6''	+25°10'46.8''
i	$51.7^\circ \pm 2.2^\circ$	$54.0^\circ \pm 0.1^\circ$
$\Phi_{\text{phot},d}$	$56.6^\circ \pm 2.6^\circ$	$50.7^\circ \pm 0.8^\circ$
$\Phi'_{\text{phot},b}$...	$92.1^\circ \pm 7.7^\circ$
ϵ_{bar}	...	0.26 ± 0.02
ϵ_{bulge}	0.00 ± 0.00	0.10 ± 0.12
$I_{e,\text{bulge}}$	3.69 ± 1.88	1.84 ± 0.89
$I_{e,\text{disk}}$	0.17 ± 0.03	0.19 ± 0.02
$r_{e,\text{bulge}} [\text{arcsec}]$	1.38 ± 0.63	2.42 ± 0.48
$r_{e,\text{disk}} [\text{arcsec}]$	36.08 ± 5.67	17.05 ± 1.81
n_{bulge}	1.05 ± 0.61	0.46 ± 0.17
n_{disk}	1.59 ± 0.15	1.50 ± 0.06
Per cent disk	93.94 ± 3.15	67.53 ± 8.20
Per cent bulge	6.06 ± 3.15	18.16 ± 9.26
Per cent bar	...	14.31 ± 7.06

the bar and is likely associated with strong non-circular gas motions caused by the bar. However, we do not observe the change of sign beyond the $10''$ radius reported by Zasov et al. (2019). We performed non-linear least-squares fitting to the rotation curves following Courteau (1997) arctan function modified to account for a possible increase/decline in the rotational velocity at high galactocentric radii (Drew et al. 2018) :

$$\bar{V}_t(r) = \frac{2}{\pi} V_a \arctan\left(\frac{r}{r_t}\right) + cr \quad (2)$$

where V_a is an asymptotic velocity, c is the outer slope and r_t is a transition radius between the rising inner part and outer part. Fits to the rotation curves with this function are represented by dashed lines in Fig. 5g and Fig. 5h.

DiskFit can also be used to fit axisymmetric and non-axisymmetric

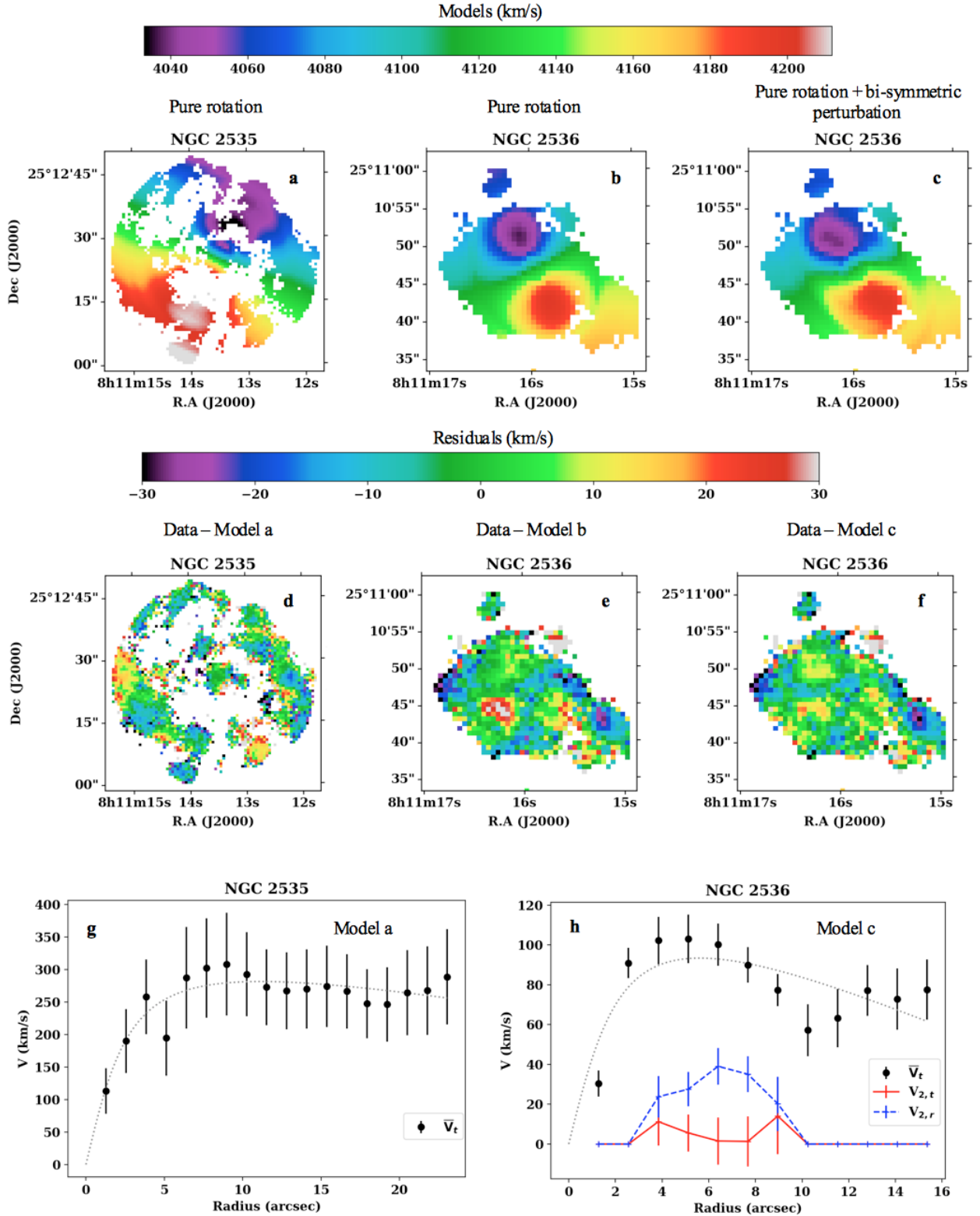


FIGURE 5. Fitted velocity models for the H α velocity fields. (a - c) : Rotation-only models for NGC 2535 and NGC 2536 and rotation+bi-symmetric flow model for NGC 2536. (d - f) : corresponding residuals. (g, h) : Rotation curves correspond to the best-fitting models, i.e rotation-only model for NGC 2535 and rotation+bi-symmetric flow for NGC 2536. The dotted lines are arctan functional fits to the rotation curves (see text).

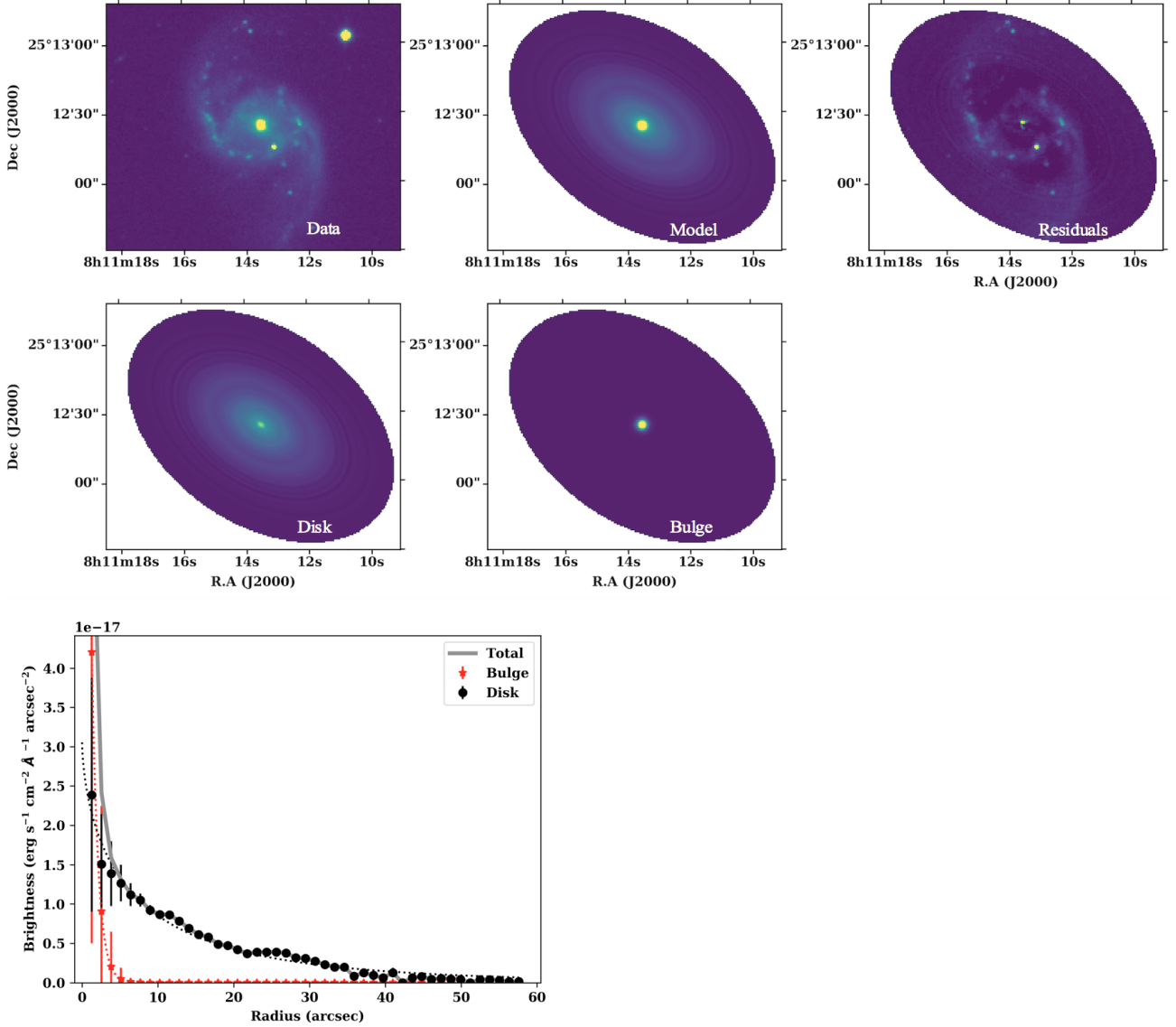


FIGURE 6. SN3 band continuum model for NGC 2535. Top left : SN3 continuum image of NGC 2535; top centre : disk+bulge DiskFit model; top right : (data-model) residuals; middle left : disk component of the model; middle centre : bulge component of the model; bottom : radial brightness distribution of the model components. Dashed lines are fits to brightness profiles with an exponential function (Eq. (3))

models to images. We model the continuum map since it is smoother than the $H\alpha$ flux map. The photometry branch of the code can fit up to three components simultaneously : a disk, a bar and a bulge. The code determines the best-fitting values for (x_c, y_c) , disk PA, disk ellipticity (and corresponding inclination), bar PA, bar ellipticity. The only component that has an assumed light profile is the bulge, which is parameterized by a Sérsic function :

$$I(r) = I_e \exp \left\{ -b_n \left[\left(\frac{r}{r_e} \right)^{1/n} - 1 \right] \right\} \quad (3)$$

where I_e is the brightness at the effective radius r_e , n is the Sérsic index. The factor b_n is a function of the shape parameter, n , such that $\Gamma(2n) = 2\gamma(2n, b_n)$, where Γ is the gamma function and γ is the incomplete gamma function. The bulge is spheroidal with an apparent ellipticity ϵ_{bulge} , with the disk plane being the plane of symmetry.

Fig. 6 and Fig. 7 show the best photometric models and residuals

to the SN3 band continuum map together with the corresponding brightness profiles. The black dashed lines in the bottom panel represent non-linear least squares fits to disk brightness profiles by Eq. (3). The best fitting photometric parameters are listed in Table 3. 100 bootstrap realizations of each photometric model were used to estimate the uncertainties on the photometric parameters.

We fit a bulge+disk+bar model for NGC 2536. The resulting bar has the appearance of a ring while the enclosed bulge has a Sérsic index characteristic of bars ($n = 0.5$). The bulge and the bar contribute up to 32% of the total brightness of the model. The residuals are higher for star-forming knots in the bar and bulge. The photometric centre, inclination and PAs values are very close to those derived from the analysis of velocity maps. The stellar mass of the galaxy may be estimated from its $(g-i)$ and $(i-H)$ colours (Zibetti et al. 2009). From the SIMBAD astronomical data base, $(g-i) = 0.75$ and $(i-H) = 2.0$ which results in $M/L_H \sim 0.25$. Considering the adopted distance of 59.2 Mpc, $L_H = 1.3 \times 10^{10} L_\odot$ or $M_\star = 3.2 \times 10^9 M_\odot$.

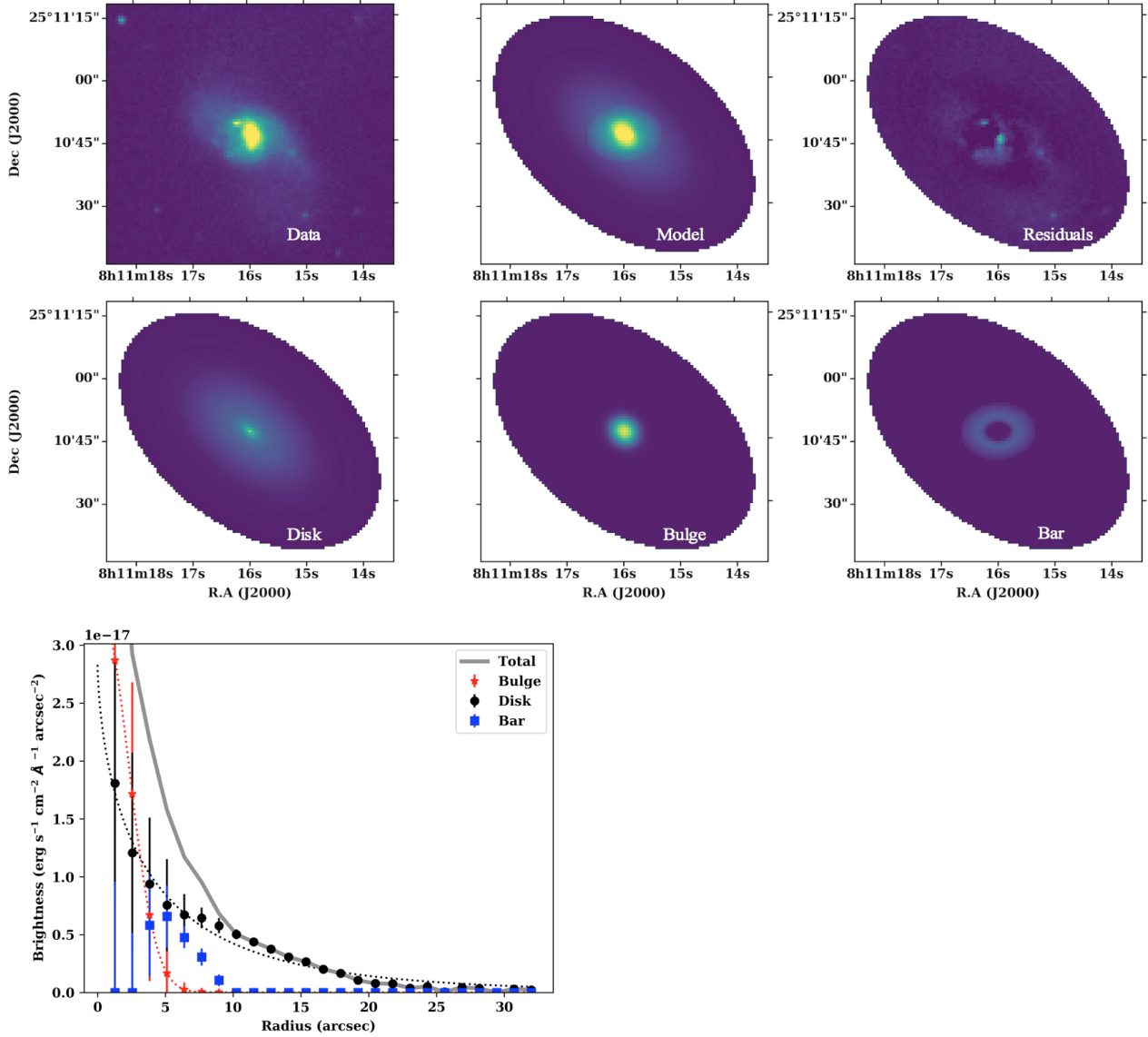


FIGURE 7. Same as in Fig. 6 but for NGC 2536. Top left : SN3 continuum image of NGC 2536; top centre : disk+bulge+bar DiskFit model; top right : (data–model) residuals; middle left : disk component of the model; middle centre : bulge component of the model; middle left : bar component of the model; bottom : radial brightness distribution of the model components. Dashed lines are fits to brightness profiles with an exponential function (Eq. (3))

The total HI mass of Arp 82 is $2.4 \times 10^{10} M_{\odot}$, of which $2.4 \times 10^9 M_{\odot}$ is associated to NGC 2536 (Kaufman et al. 1997). The dynamical mass can be estimated as $M_{\text{dyn}}(r) = (V^2 + 3.36\sigma^2 r/r_e) \times r/G$ where G is the gravitational constant, V is the rotational velocity, σ is the isotropic velocity dispersion (Drew et al. 2018). Kaufman et al. (1997) report velocity dispersions of ~ 30 km/s all over the system for the HI gas. We measure velocity dispersions of about the same value (see Fig. A1) for the ionized gas in star forming knots with the highest SNR. Assuming $\sigma = 30$ km/s and $V(r_e) = 54$ km/s (inferred from the parameterized rotation curve) we find a dynamical mass of $6.5 \times 10^9 M_{\odot}$ enclosed in one effective radius.

For NGC 2535, we fit a bulge+disk model to the data. The bulge has a Sérsic index $n_{\text{bulge}} = 1$, characteristic of disks. The bulge contributes only 6% to the model total brightness. The ocular ring and the tidal arms stand out in the residuals image. For this galaxy, we infer $V(r_e) = 210$ km/s, corresponding to a dynamical mass of $1.1 \times 10^{11} M_{\odot}$ within a radius $r = r_e$. However, the photometric inclination

and PA of the disk are very different from the equivalent kinematic parameters values. If the inclination deduced from the image analysis is correct, $V(r_e)$ would be a factor $\sin 51.7/\sin 18.1 = 2.5$ less and the above estimated dynamical mass would be $2.5 \times 10^{10} M_{\odot}$. (g–i) and (i–H) colours from SIMBAD (1.20 and 2.23 respectively) suggest a $M/L_H \sim 0.25$ or $M_{\star} = 5.4 \times 10^{10} M_{\odot}$. Thus, the photometric inclination is certainly not correct as the computed dynamical mass would be less than the baryonic mass. This explains the very low dynamical mass, comparable to the HI content of the system, deduced from the H α Fabry-Perot observations by Amram et al. (1989) who found an inclination $i = 43^\circ \pm 10^\circ$ based on the ellipticity of the inner isophotes. Kaufman et al. (1997), using the Persic & Salucci (1991) relation adopt an inclination $i = 23^\circ \pm 4^\circ$ to get velocities consistent with the B band luminosity of NGC 2535. The kinematic inclination is therefore favored. Hence, the galaxy disk and the eye-shaped ring with a major axis at $117^\circ \pm 12^\circ$ all have intrinsic elliptical shapes. The misalignment between the kinematic and photometric PAs and the

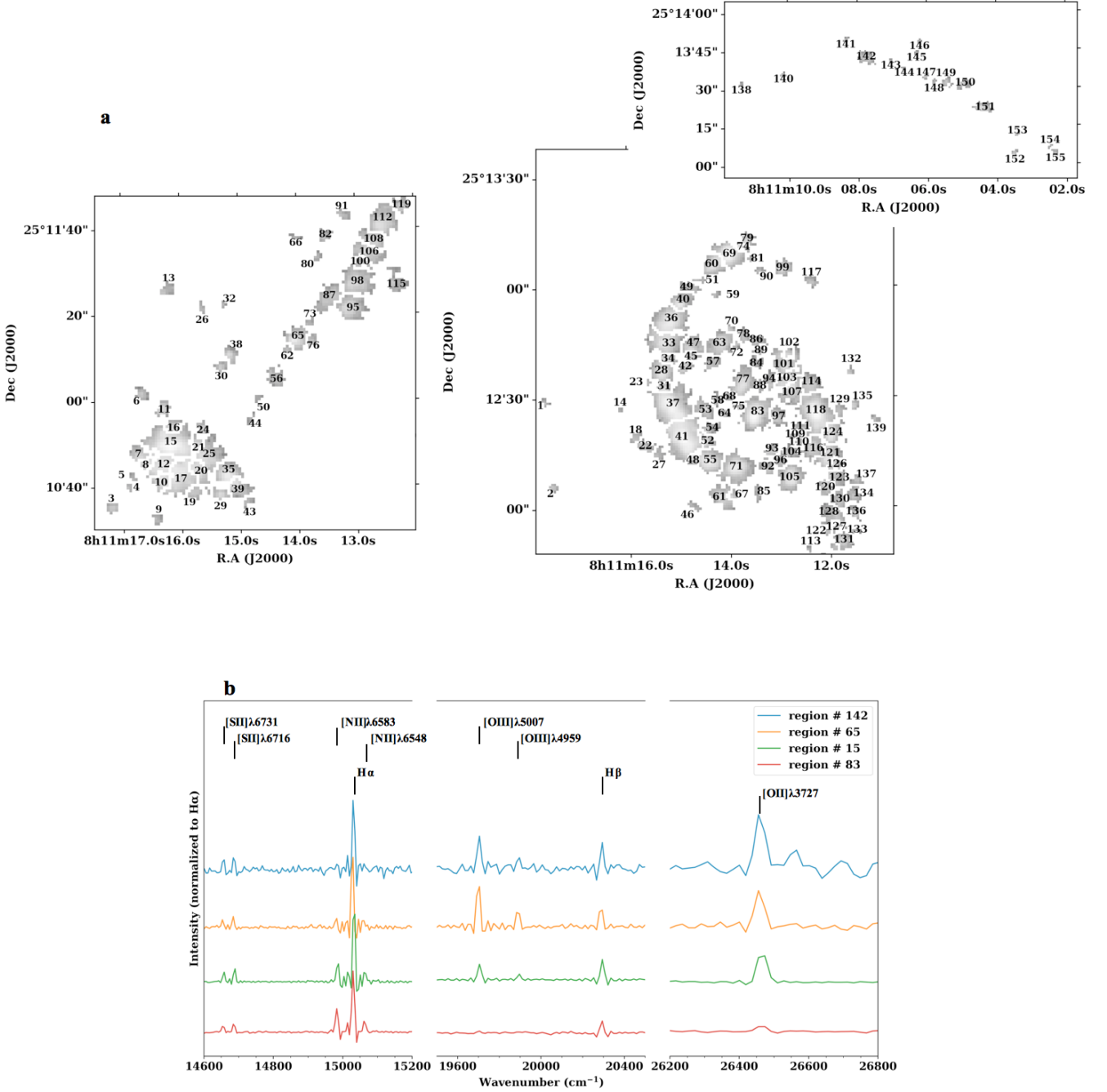


FIGURE 8. (a) HII region complexes detected in NGC 2536 and the bridge (left) and in NGC 2535 (right). (b) Spectra of regions #143 (in the extended northern arm of NGC 2535), 65 (in the bridge), 15 (in the centre of NGC 2536) and 83 (in the centre of NGC 2535). Variations in the relative strength of high and low-ionization emission lines with respect to the Balmer lines hints for differences in metallicity.

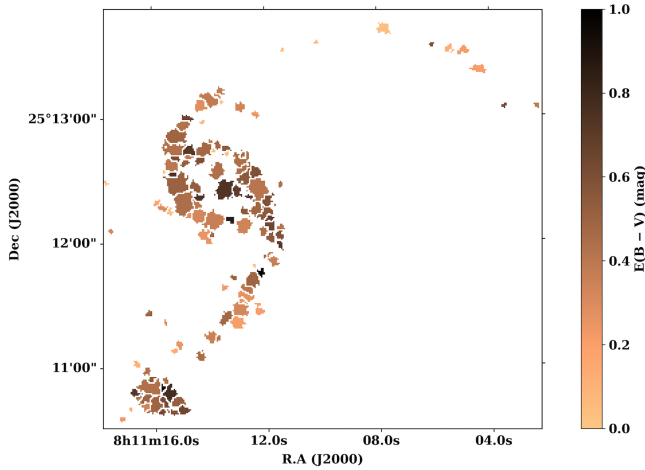
intrinsic ellipticity of the stellar disk are induced by the interaction as discussed in Section 4.

3.2 Properties of HII regions

3.2.1 Region detection and integrated spectra

Gas phase metallicity is generally traced through oxygen abundance. Ionized gas oxygen abundances have been well calibrated on the basis of strong-line indicators for ionized regions associated with

SF processes. We have selected HII region complexes using the automated HIIPhot algorithm (Thilker et al. 2000, 2002). The procedure applied on the H α emission line and continuum maps detects 155 sources above the 10σ level. The selected HII region complexes are shown in Fig. 8a. Positions and fluxes of the detected regions can be found in Table A1. Fluxes of the HII region complexes are then extracted from their sky subtracted integrated spectra in the same manner described in Section 2, i.e. emission lines are fitted using sinc profiles for the SN1, SN2 data cubes and sincgauss profiles for the SN3 data cube. Visual inspection of the spectra do not show any

FIGURE 9. $E(B - V)$ map.

significant underlying Balmer absorption. We, therefore, do not subtract any model stellar spectra from the extracted integrated spectra. Fig. 8b illustrates spectra of some bright regions detected near the galaxy centres (regions #15 and 83) and in the tidal tails (regions #65 and 142). We corrected extracted fluxes for Galactic extinction and internal dust attenuation derived from the Balmer decrement $H\alpha/H\beta$. For the Galactic extinction, we assume the Cardelli extinction law (Cardelli et al. 1989) with $R_V = 3.1$ and $A_V = 0.117$, as provided by the NED astronomical database. For the internal dust attenuation, we assume a Calzetti law (Calzetti 2001) and a theoretical $H\alpha/H\beta = 2.86$ for the Case B recombination at $T = 10\,000\text{ K}$, $n_e = 100\text{ cm}^{-3}$ (Osterbrock & Ferland 2006). We discard 40 regions with $H\alpha$ or $H\beta$ fluxes with a $\text{SNR} \leq 3$. The resulting color excess $E(B - V)$ map is shown in Fig. 9 with a median value of ~ 0.44 .

Selecting regions solely based on their brightness, however, does not provide information on the ionization mechanisms. In order to exclude sources other than SF processes, we need to inspect their locations on the BPT diagrams (Baldwin et al. 1981). To this purpose, we only consider regions with a $\text{SNR} > 3$ for all emission lines before doing the diagnostic. This process further excludes 45 regions. Thus, of the 155 regions detected with HIIphot, we finally only keep 70. The $[\text{NII}]\lambda 6583/H\alpha$ vs. $[\text{OIII}]\lambda 5007/H\beta$ and $[\text{SII}]\lambda 6716, 6731/H\alpha$ vs. $[\text{OIII}]\lambda 5007/H\beta$ diagnostic line ratios are shown in Fig. 10. All selected regions lie leftward (within uncertainties) of the demarcation lines in the BPT diagrams (Fig. 10).

3.2.2 Oxygen abundance determination

To evaluate gas phase metallicity, we chose five different calibrators widely used in the literature, and compare the derived abundances to avoid systematic biases that may arise from the adopted extinction, diffuse ionized gas (DIG) contribution, low ionization emission regions (LIERs), ionization parameter or relative elemental abundances variations (e.g., N/O variations when using indicators based on $[\text{NII}]$ emission lines to derive metallicity). Those indicators are N2Ha (Kobulnicky & Kewley 2004; Marino et al. 2013), based on $([\text{NII}]\lambda 6583/H\alpha)$, O3N2 (Marino et al. 2013), based on $([\text{OIII}]\lambda 5007/H\beta)/([\text{NII}]\lambda 6583/H\alpha)$ line ratio, N2O2 (Kewley & Dopita 2002; Bresolin 2007), based on $[\text{NII}]\lambda 6583/([\text{OII}]\lambda 3727, 3729)$ line ratio and R23 (Kobulnicky & Kewley 2004), based on $([\text{OII}]\lambda 3727, 3729 + [\text{OIII}]\lambda 5007)/H\beta$

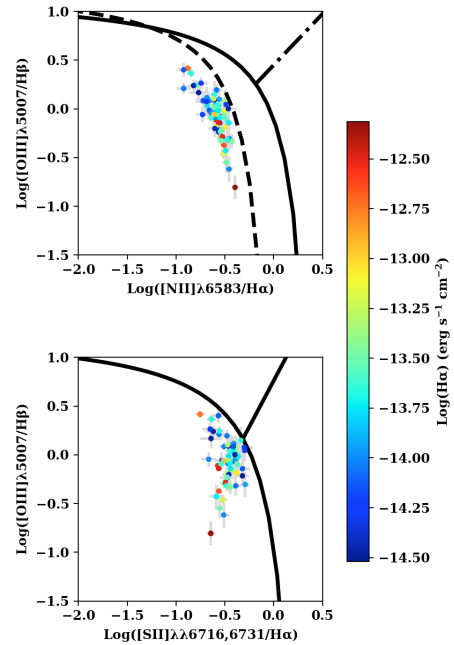


FIGURE 10. BPT diagrams showing excitation properties of detected HII regions (see text). Demarcation lines from Kewley et al. (2001) (solid lines), Kauffmann et al. (2003) (dashed line), Schawinski et al. (2007) (dash-dotted line) are plotted and separate star forming regions, high ionization and low ionization emission regions. Color denotes extinction corrected $H\alpha$ fluxes.

line ratio. N2Ha is not sensitive to reddening correction or flux calibration as the involved lines are very close in wavelength but is particularly sensitive to the ionization parameter and to the presence of strong shock excitation or DIG/LIERs contribution. The indicator scales linearly with nitrogen abundance at low metallicities ($\text{N2Ha} < -0.8$) but saturates at high metallicities (Kewley & Dopita 2002). Kumari et al. (2019) have shown that the O3N2 indicator is not significantly affected by DIG/LIERs. The indicator also has the advantage to vary monotonically with metallicity. However, the diagnostic ratio is affected by variations in the ionization parameter since $[\text{NII}]$ and $[\text{OIII}]$ originate from ions with a large difference in ionization potential. N2O2 , on the other hand, is ionization parameter independent and is a good diagnostic, but only for metallicities above half solar (Kewley & Dopita 2002). The R23 parameter has a local maximum and is often used in conjunction with another indicator like N2O2 and an ionization parameter estimator like the O3O2 ($\log([\text{OIII}]\lambda 5007/([\text{OII}]\lambda 3727, 3729))$) and gives reliable estimates of oxygen abundances at low metallicities. For O3N2 , we used the empirical calibration of Marino et al. (2013), valid for $-1 < \log([[\text{OIII}]\lambda 5007/H\beta)/([\text{NII}]\lambda 6583/H\alpha)] < 1.7$ (all HII region complexes analyzed here fall in this range). For the N2O2 diagnostic, we used the theoretical calibration provided by Kewley & Dopita (2002) for regions with $12 + \log(\text{O}/\text{H}) > 8.6$ or $\log([\text{NII}]\lambda 6583/([\text{OII}]\lambda 3727, 3729)) > -0.97$. For $\log([\text{NII}]\lambda 6583/([\text{OII}]\lambda 3727, 3729)) < -0.97$ we used the empirical Bresolin (2007) prescription. For R23 , we used the iterative procedure described in Kobulnicky & Kewley (2004) to derive (O/H) abundances and the ionization parameter simultaneously. For N2Ha , we adopt the parameterization given by Kobulnicky & Kewley (2004) (N2Ha_KK04 hereafter) and use the final ionization parameter map obtained by the R23 calibration to derive (O/H) . We also use the Marino et al. (2013) empirical calibration (N2Ha_M13) for

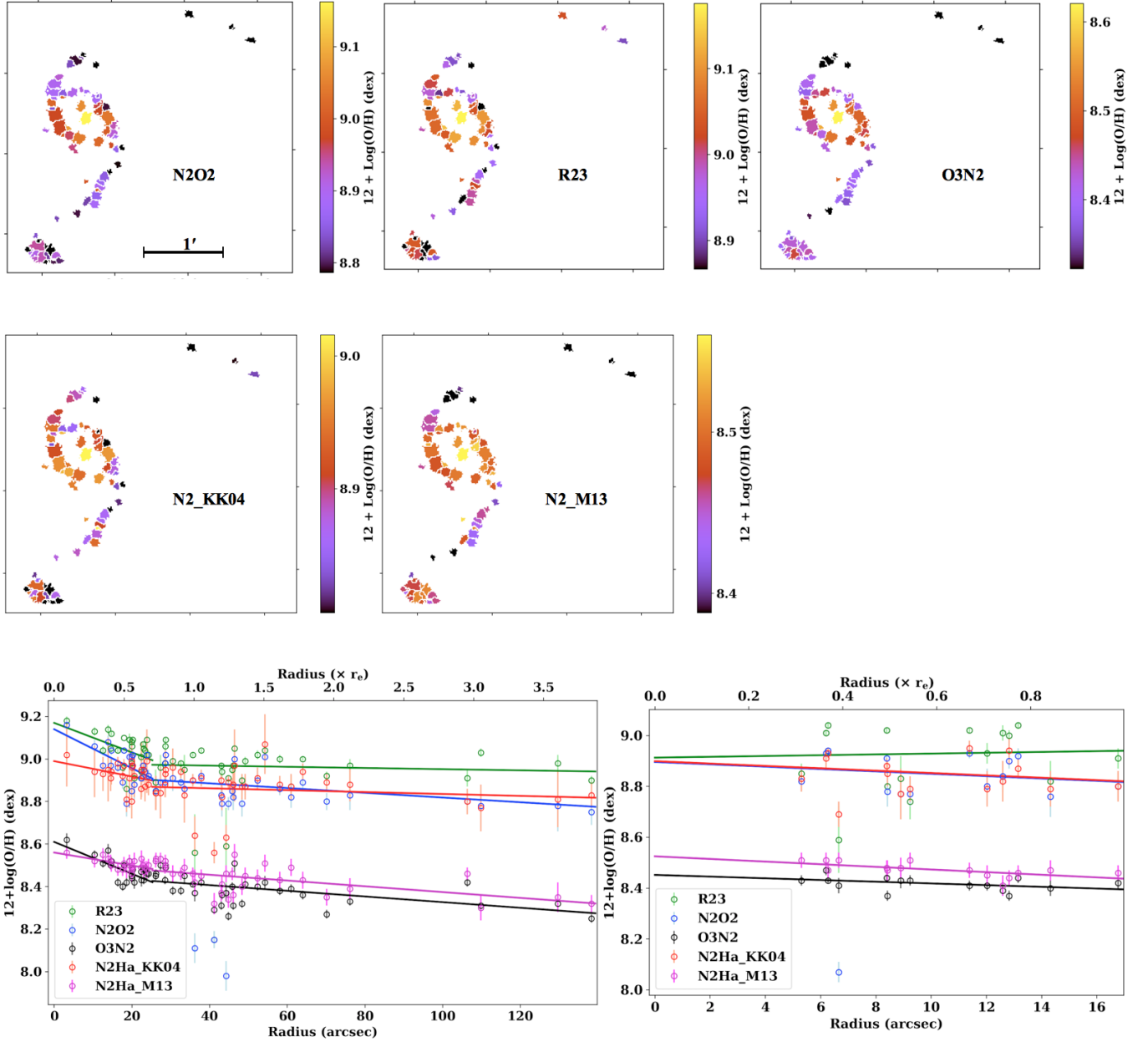


FIGURE 11. Abundance maps (top and middle panels) and abundance profiles (lower panel) for NGC 2535 and NGC 2536. The maps and profiles are obtained for the N2O2, R23 and O3N2, N2Ha_KK04 and N2Ha_M13 calibrations. Linear fits (solid lines) to the data points are performed ignoring outliers (see text).

the same indicator. (O/H) abundance maps derived using the five different methods are reproduced in Fig. 11 together with the (O/H) radial distribution in the disks of NGC 2535 and NGC 2536. Deprojected galactocentric distances were computed taking into account the kinematical PAs and inclinations found in Section 3.1. Absolute metallicity estimates from the five calibrations are different with systematically lower values obtained for the empirical calibrations (O3N2 and N2Ha_M13). This discrepancy is expected as theoretical calibrations usually lead to higher (O/H) values than empirical ones (Kewley & Ellison 2008)¹. This also explains the low values found

for region #21 in NGC 2536 and regions #99, 119, 134 in NGC 2535 where the empirical calibration of Bresolin (2007) was used for the N2O2 indicator. The corresponding R23 values are also low as N2O2 values serve as initial guesses for this calibrator. We find an offset of ~ 0.5 dex between the theoretical and empirical calibrations. The O3N2 values are less scattered in the radius vs. (O/H) diagrams. Cen-

state-of-the-art models that assume empirical laws between O/H, ionization parameter and N/O (e.g., Pérez-Montero 2014) give chemical abundances in good agreement with those derived from the direct method for high metallicity objects. On the other hand, some recent empirical calibrations (e.g., Pilyugin & Grebel 2016) provide estimates of abundances also compatible with those from the direct method.

¹ However, we note that, on the one hand, some tailor-made models for low metallicity objects (e.g., Pérez-Montero et al. 2010) and some recent

tral values of oxygen abundance found using the O3N2 calibration are in agreement with those derived by [Zasov et al. \(2019\)](#) who accounted for underlying stellar absorption in measuring emission line fluxes. Had the underlying H β absorption line been important and not detected in our spectra due to the low resolution of the SN2 cube, we would have underestimated the H β fluxes. As a consequence, we would have overestimated the internal extinction and significantly underestimated central oxygen abundances.

3.2.3 Galactocentric abundance gradients

Spatial distribution of oxygen abundance in the disk of NGC 2535 exhibits two slopes for all the methods used. The break occurs at $\sim 25''$, just beyond the ocular ring. Indeed, the tidal tails have constant metallicity over long patches in the abundance maps. This is in agreement with the nearly constant abundance along the tidal bridge observed by [Zasov et al. \(2019\)](#). Linear least-squares fit give slopes of 0.04 ± 0.02 , -0.05 ± 0.02 , -0.04 ± 0.01 , -0.02 ± 0.02 , -0.05 ± 0.01 dex/ r_e for N2O2, R23, O3N2, N2Ha_KK04, N2Ha_M13 calibrations respectively. Regions #21, 99, 119, 134 were considered as outliers and were not used in the fits since they depart considerably from the general trend observed for the other regions for the N2O2 and R23 calibrators. Inside the ocular ring, the slope is steeper. We find gradients of -0.33 ± 0.11 , -0.25 ± 0.10 , -0.27 ± 0.06 , -0.13 ± 0.08 , -0.11 ± 0.03 dex/ r_e with central (O/H) abundances of 9.14 ± 0.05 , 9.17 ± 0.05 , 8.61 ± 0.03 dex for N2O2, R23, O3N2, N2Ha_KK04, N2Ha_M13 calibrations respectively. The inner slope is a bit less steep for the N2Ha calibrator since it saturates at high metallicities but the break in the O/H distribution is clear. The slopes derived are consistent within errors. The lower (O/H) values in the tidal tails suggest that these features are made of gas expelled from the disk periphery. In NGC 2536, the oxygen abundance distribution can be fitted with a single slope. We find gradients of -0.08 ± 0.09 , 0.02 ± 0.15 , -0.05 ± 0.03 , -0.08 ± 0.08 , -0.08 ± 0.03 dex/ r_e with central abundances of 8.89 ± 0.06 , 8.91 ± 0.09 , 8.45 ± 0.02 , 8.89 ± 0.05 , 8.52 ± 0.02 dex for N2O2, R23, O3N2, N2Ha_KK04, N2Ha_M13 calibrations respectively. The slopes derived for NGC 2536 are also consistent within errors. It is interesting to note that central metallicity in NGC 2536 is higher compared to the metallicity in the bridge, suggesting that the gas in the satellite galaxy has not yet mixed with the gas in the tidal bridge. [Sánchez et al. \(2014\)](#) showed that, when using the O3N2 indicator, disk galaxies in the local universe present a common gradient in the oxygen abundance of ~ -0.1 dex/ r_e up to ~ 2 effective radii beyond which the distribution flattens out. The characteristic gradient is independent of morphology, presence or absence of bars, absolute magnitude, or stellar mass. Only interacting galaxies in their sample show clear deviations from the common gradient with an average slope of -0.05 dex/ r_e . This is the case with the average slope derived for NGC 2536. For NGC 2535, only the outer slope is significantly shallow to this standard. Flat slopes in tidal debris have also been observed in other interacting systems ([Weilbacher et al. 2003](#); [Torres-Flores et al. 2014](#)). Since a metallicity gradient is expected at radii $< 2r_e$ for non-interacting disk galaxies, the flat outer slope hints at some mixing in the tidal debris or tidal stretching induced by the interaction. At this early stage of the interaction, tidal stretching seems more likely to cause the flattening.

3.2.4 Nucleus and star formation rate

We do not detect any signature of AGN in our data. Inspection of the velocity dispersion map in Fig. A1 shows that a maximum of ~ 45

km/s is reached in the centre of NGC 2535. This value is very low compared to velocity dispersion of a few hundreds km/s observed in narrow line regions (NLRs) of active galaxies. It is even lower if compared to the widths of broad line regions. Extended NLRs would have similar widths but emission lines from the integrated spectra do not suggest the presence of multiple components associated to AGN-driven outflows/inflows and the diagnostic line ratios of Fig. 10 do not show any evidence of an AGN source. Although AGNs may be optically elusive, NIR spectra obtained by [Lee et al. \(2012\)](#) do not show any AGN signature either. The total H α luminosity of the region complexes is 1.5×10^{42} erg s $^{-1}$ for the adopted distance. The brightest regions are located at the centres of the galaxies, at the apices of the ocular and at the tip of the north spiral arm of NGC 2535. Half of the total H α luminosity is contributed by regions in the ocular. The proportion rises to seventy percent when accounting the spiral arms attached to the eye-shaped ring whereas the luminosity in the tidal tails amounts to five percent. Assuming that H α luminosity is totally due to SF, we compute a global SFR of $8.1 M_{\odot}$ yr $^{-1}$ for the Arp 82 system using the [Murphy et al. \(2011\)](#) calibration. The SFR would be $12.1 M_{\odot}$ yr $^{-1}$ were it computed using [Kennicutt \(1998\)](#) calibration due to differences in stellar initial mass functions (IMF) and stellar population models (instantaneous vs. continuous SF) assumptions. The total infrared luminosity ($L_{\text{IR}} = 1.1 \times 10^{44}$ erg s $^{-1}$) suggests a SFR measurement consistent with that traced by the H α luminosity when considering the ([Buat & Xu 1996](#)) relation valid for galaxies of type Sb and later. The derived SFR and total stellar mass (previous section) place the system on the local blue SDSS galaxies sequence in the SFR- M_{\star} diagram of [Elbaz et al. \(2007\)](#) (see their Fig. 18 and Eq.5). Hence, the SF activity of Arp 82 is still comparable to typical star forming galaxies at $z = 0$ with the same stellar mass.

4 NUMERICAL MODEL

4.1 Simulation code

To simulate the collision between the two galaxies, we used the galactic chemodynamical evolution code GCD+ ([Kawata & Gibson 2003](#); [Kawata et al. 2013](#)). GCD+ is a 3D tree N-body/SPH code that incorporates self-gravity, hydrodynamics, radiative cooling, star formation, supernova feedback, metal enrichment, and metal diffusion. Star formation occurs whenever the local number density of gas is greater than a threshold n_{th} , the gas velocity field is convergent, and the gas is Jeans unstable following the Schmidt law :

$$\frac{d\rho_{\star}}{dt} = \frac{d\rho_g}{dt} = \frac{C_{\star}\rho_g}{t_g}, \quad (4)$$

where ρ_{\star} and ρ_g are the stellar and gas mass density, respectively, t_g the dynamical time and C_{\star} a dimensionless star formation efficiency. We use $n_{\text{th}} = 0.1 \text{ cm}^{-3}$ and $C_{\star} = 0.012$. Dark matter, gas, and stellar components are represented by particles. Stellar and gas particles have equal masses. Each stellar particle represents a population of stars born at the same time with stellar masses distributed according to the [Salpeter \(1955\)](#) IMF. The stellar wind (SW) energy output $E_{\text{SW}} = 10^{36}$ erg s $^{-1}$ and the supernova (SN) energy output $E_{\text{SN}} = 10^{51}$ erg with only 10% contributing to feedback, the rest being radiated away.

Since the algorithm does not include an actual treatment of ionization, we assume that ionized gas is traced by gas particles with high density and temperature (average $n_{\text{H}} > 1 \text{ cm}^{-3}$, $T > 420 \text{ K}$). The assumption is made considering that in the Galaxy, the hot and diffuse ionized gas have densities well below 1 cm^{-3} and the mass

TABLE 4. Initial properties of the simulated galaxies. DM, gas, star labels refer to the dark matter, gaseous, stellar components respectively. M , ℓ and N represent the total mass, scale length and total number of particles respectively.

Galaxy	$M_{\text{DM}} [10^9 M_\odot]$	$M_{\text{gas}} [10^9 M_\odot]$	$M_{\text{star}} [10^9 M_\odot]$	$\ell_{\text{gas}} [\text{kpc}]$	$\ell_{\text{star}} [\text{kpc}]$	N_{DM}	N_{gas}	N_{star}
Gal1	3154.265	32.304	51.504	6.0	3.0	630848	129216	206016
Gal2	492.853	2.692	4.292	2.0	1.0	98570	10768	17168

TABLE 5. Initial conditions

$\mathbf{R}_1 [\text{kpc}]$	(0,0,0)
$\mathbf{R}_2 [\text{kpc}]$	(74,20,8)
$\mathbf{V}_1 [\text{km s}^{-1}]$	(0,0,0)
$\mathbf{V}_2 [\text{km s}^{-1}]$	(-120,170,13)
$(\theta, \phi)_1$	(342,0)
$(\theta, \phi)_2$	(48,270)

weighted average temperature of the atomic gas and ionized gas by HII regions is ~ 420 K.

4.2 Initial conditions

The simulation is run assuming a Λ CDM standard cosmology with $h = 0.73$, $\Omega_0 = 0.266$, $\Omega_b = 0.044$, $\lambda_0 = 0.734$. Each galaxy is composed of a dark matter halo with a NFW profile (Navarro et al. 1996) with a concentration parameter $c = 20$, and a galactic disk with exponential density profile :

$$\rho = \frac{M}{4\pi\zeta\ell^2} \text{sech}^2\left(\frac{z}{\zeta}\right) \exp\left(-\frac{R}{\ell}\right), \quad (5)$$

where R and z are the radial and vertical coordinates, ℓ is the scale length, ζ is the scale height (set to $\ell/8$), M is the mass of the stellar/gaseous component. The initial masses, scale lengths, and number of particles for the simulated galaxies are given in Table 4. The stellar and gaseous disks of the primary and satellite galaxies have initial central iron abundances $[\text{Fe}/\text{H}]$ of 0.2 and 0 dex, respectively, with radial gradients of -0.03 and -0.06 dex/kpc respectively. α -elements are initially only present in the stellar component with abundances given by :

$$[\alpha/\text{Fe}] = -0.16[\text{Fe}/\text{H}]. \quad (6)$$

The metallicity of each particle is modified by adding a Gaussian scatter of 0.02 dex to create a local dispersion. Stellar particles are assigned an age following an age-metallicity relation $[\text{Fe}/\text{H}] = -0.04 \times \text{age}(\text{Gyr})$. The simulated interacting galaxies both rotate counterclockwise and the encounter is prograde-retrograde with initial positions, velocities and inclination angles given in Table 5.

Several simulations were run in order to reproduce the morphology, kinematics, metallicity distribution, distance, global SFR observed in Arp 82. The best match simulation was found using the parameters described above and was run for 1 Gyr. The satellite galaxy is on a bound orbit with initial positions and velocities chosen to reproduce the observed distance at the best match time. At this time, the kinematics and morphologies of the galaxies, in particular tidal tails induced by the interaction, are influenced by the choice of the initial scale lengths and initial inclinations. Initial metallicity and radial gradients were chosen to reproduce the observed metallicity distribution (derived using the N2O2 calibrator). Initial masses were chosen to reproduce the observed stellar and gaseous masses at the best match time.

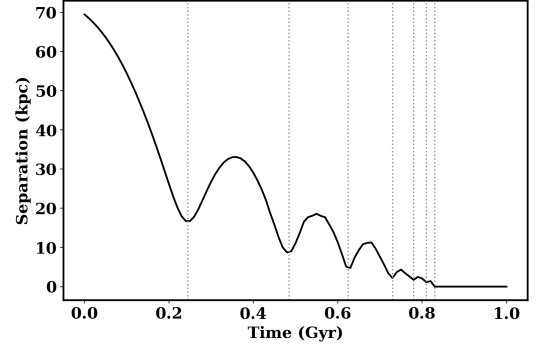


FIGURE 12. Temporal evolution of the separation between the centres of mass of the simulated interacting galaxies. Dotted lines identify instants at pericentre passages.

4.3 Simulations

To investigate the effects of the interaction, we also ran simulations of the same galaxies with the same parameters but evolved in isolation. In the following, we refer to the primary and secondary galaxies as Gal1int and Gal2int, if simulated in interaction, and Gal1iso and Gal2iso when they are evolved in isolation.

Gal1int and Gal2int are initially separated by ~ 70 kpc and experience several close passages in their encounter before merging at $t = 0.83$ Gyr as shown in Fig. 12. The best match to the observations occurs at $t = 0.39$ Gyr, just past the first apocentre, when the distance (30.6 kpc) between Gal1int and Gal2int very well matches the measured separation between NGC 2535 and NGC 2536. We thus identify $t = 0.39$ Gyr as “the present”.

4.3.1 Formation and evolution of tidal features

Fig. 13 illustrates the time evolution of the configuration of the stellar particles in three orthogonal (xy , yz , xz) projections. The xy plane is adopted as the plane of the sky and all particles are rotated by 15° in this plane around the origin after the run. The interaction strengthens spiral arms in Gal1int and tidal forces elongate the stellar disks as Gal1int and Gal2int approach the first pericentre passage. The elongation of Gal1int in the direction joining the centres of the interacting galaxies at first pericentre passage explains the intrinsic ellipticity and photometric P.A. observed for the stellar disk of NGC 2535. The distortion increases as the interaction progresses, with the outer parts of the disks being swept up in the tidal tails. The top right panel of Fig. 13 and its close up view in the xy plane shown in the bottom right panel show the best match stellar configuration to the observed interacting galaxies and happens when the satellite galaxy is past the first pericentre, half way to the second closest passage. Besides the strong tidal arms, Gal1int has an ocular ring and spurs which result from spiral arms existing at earlier times. The spur that crosses the bridge between Gal1int and Gal2int and the spur above the ocular ring, together with the bases of the tidal arms delineates an elliptical arc. The elliptical arc, as described by

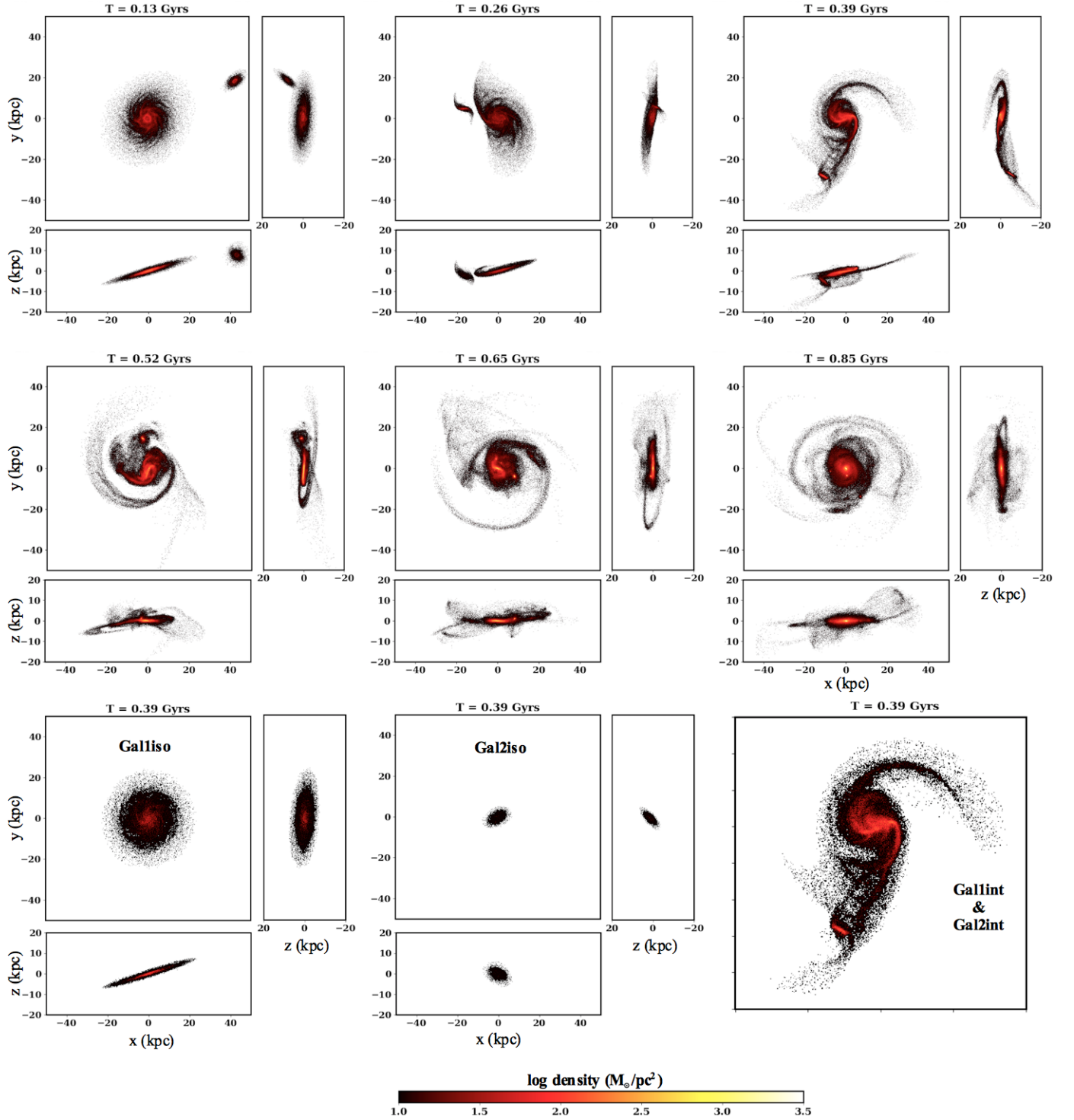


FIGURE 13. Temporal evolution of the stellar component of the simulated galaxies. Snapshots in the top and middle panels represent surface density maps of simulated interacting galaxies at selected times in the xy , yz and xz planes. The xy plane is the plane of the sky. The best match configuration to observations occurs at $t = 0.39$ Gyr; it is best shown in the xy plane in the lowest rightmost snapshot. The lowest left and middle snapshots represent stellar surface density maps of the galaxies evolved in isolation at $t = 0.39$ Gyr.

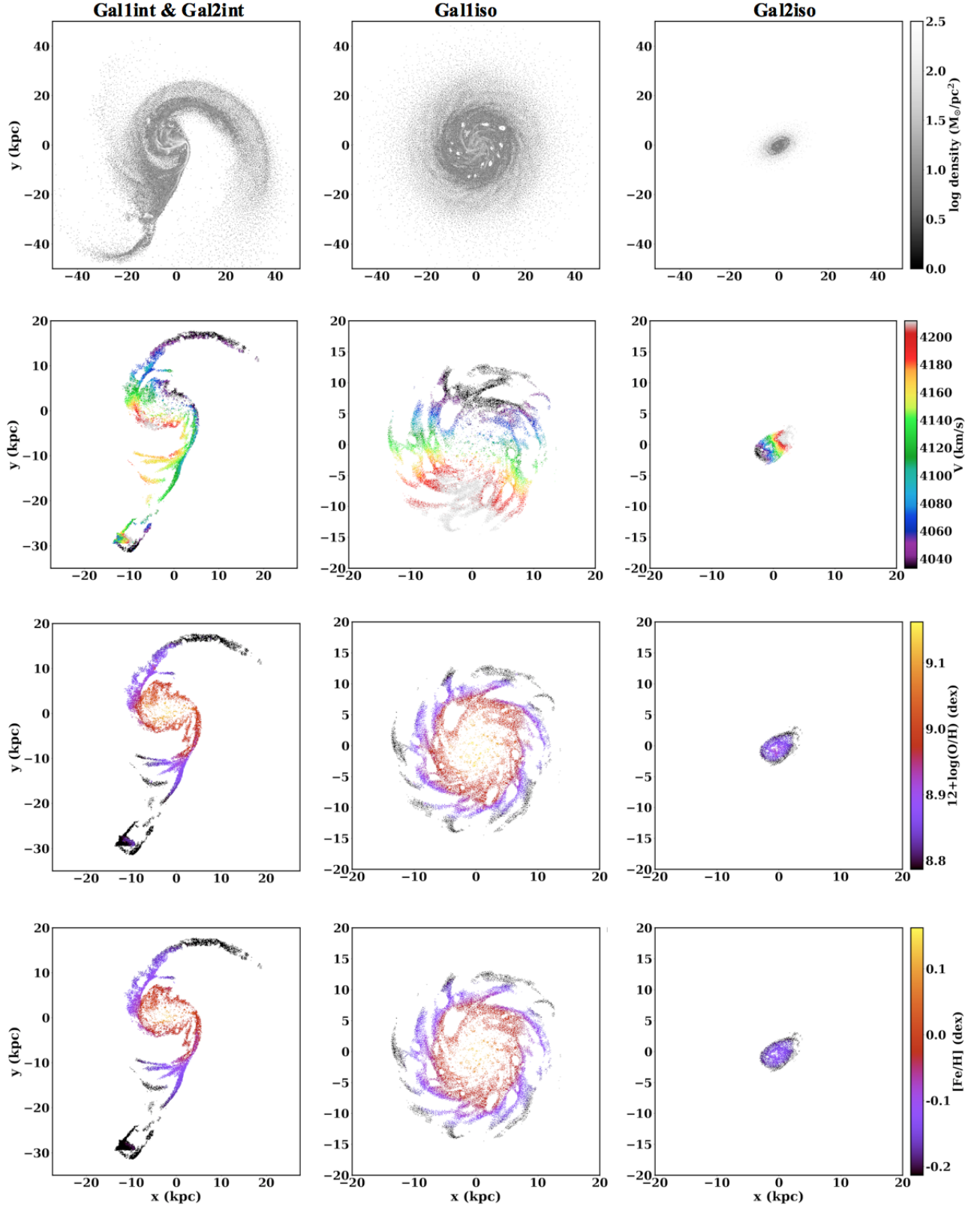


FIGURE 14. Gas surface density maps (1st row), ionized gas velocity maps (2nd row), oxygen abundance maps (3rd row) and iron abundance maps (4th row) for the simulated galaxies at $t = 0.39$ Gyr.

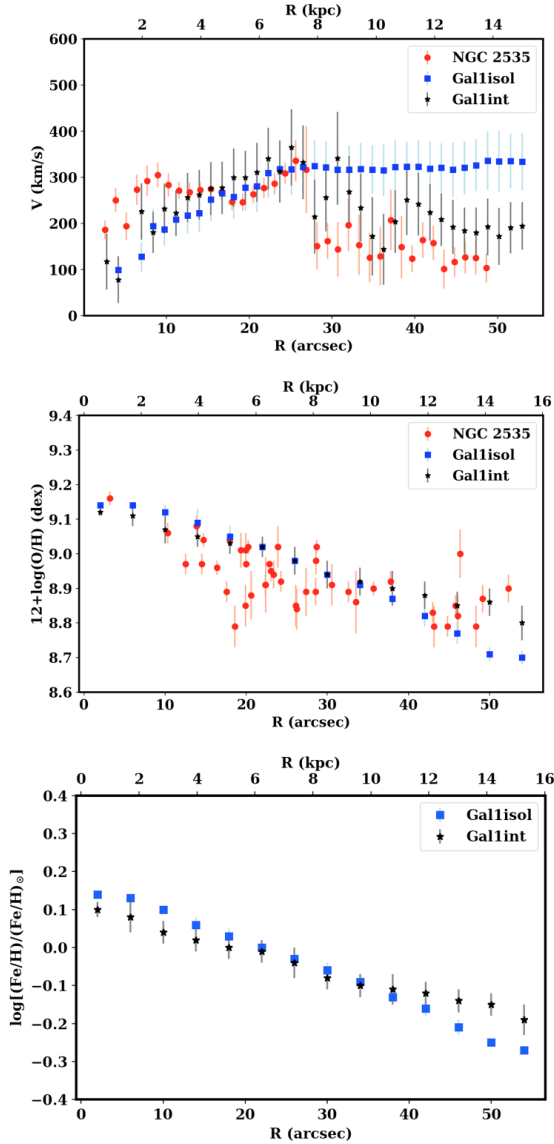


FIGURE 15. Velocity profiles (upper panel) and oxygen abundance profiles (middle panel) of Gal1int, Gal1iso, at $t = 0.39$ Gyr, and NGC 2535. The bottom panel shows the corresponding iron abundance profiles of Gal1int and Gal2int.

Kaufman et al. (1997), was not detected in their B-band and I-band images despite being similar in shape and orientation to the outer isophotes of the stellar disk of NGC 2535 in those images. This lead the authors to suggest that this structure was a purely gaseous feature resulting from a wake in the gas caused by the passage of the companion within or close to the extended HI envelope of NGC 2535. The stellar counterpart, as reproduced by our simulations, can be seen in the deep images of Fig. 1; the curved spurs of star-forming regions crossing the tidal tails are the brightest parts of the arc at its eastern and western boundaries. The structure was also detected in the UV images of Hancock et al. (2007). The simulated isolated galaxies at $t = 0.39$ Gyr are shown in the bottom left and bottom middle panels of Fig. 13. The regular circular disks of Gal1iso and Gal2iso contrast those of Gal1int and Gal2int and merely change their morphologies during the first 1 Gyr of evolution. The central

densities of Gal1int and Gal2int increase significantly past the second pericentre passage at $t = 0.49$ Gyr as their separation shortens. The simulated interacting galaxies merge at $t = 0.83$ Gyr to form a puffy remnant with shells and extended tidal arms. Although the best match to the observations happens at $t = 0.39$ Gyr, we point out that Gal1int's extended tidal arm, on the anti-companion side, is not as open as in NGC 2535. Moreover, Gal2int is not barred but this is due to the mild resolution of our simulation (see discussion on the effect of resolution in Section 4.3.6 below).

4.3.2 Kinematics and metal abundances

The best match configuration for the gaseous component is presented in Fig. 14. The upper panel shows surface density maps of the simulated galaxies. The other panels show the velocity maps, oxygen abundance maps, iron abundance maps, respectively for the same galaxies, but only considering ionized gas. The ionized gas is confined in the tidal features described above at $t = 0.39$ Gyr. The velocity maps are obtained by plotting v_z of the gas particles to which we add the average (4121 km s^{-1}) of the systemic velocities found for NGC 2535 and NGC 2536. Before the first pericentre passage, the lines of nodes of both Gal1int and Gal2int lie almost in the same direction. After the first pericentre passage, the gaseous disk of Gal2int experiences multiple deformations and is shattered, losing big chunks in its periphery which latter re-accrete making it difficult to analyze its rotation even though the central part of Gal2int in the velocity map in Fig. 14 seems to indicate normal rotation. In the metallicity maps, the gas re-accreting on Gal2int have a slightly lower metallicity than the central part which exhibits an almost uniform value caused by mixing. The gaseous debris do not accumulate at the tip of any tidal tail to form massive TDGs. Nevertheless, gaseous condensations form after the third pericentre passage. Corresponding overdensities in the stellar component can be seen in the snapshots of Fig. 13 at $t = 0.65$ Gyr near positions $(-1, 4.5)$, $(2.5, 2.5)$, and $(16, 4.5)$, and $t = 0.85$ Gyr near positions $(-8, -1)$, $(0, -3.5)$, and $(6.5, -13.5)$. These objects survive until the end of the run. For Gal1int, the differential rotation is still distinguishable up until the second pericentre passage. The line of nodes lies almost in the direction joining the centres of Gal1int and Gal2int at the best match configuration. This explains the offset between the kinematic and photometric PAs in NGC 2535. After the second pericentre passage, the difference between velocities of the receding and approaching sides diminishes considerably, leaving at the end of the run a slow rotating remnant. The simulation reproduces satisfactorily the velocity and O/H distributions of NGC 2535 when comparing the velocity maps and O/H map of Gal1int in Fig. 14 to those of NGC 2535 presented in Fig. 4 and Fig. 11.

4.3.3 Local properties

To investigate the local effects of the interaction, we conduct a radial profile analysis of the 2D velocity maps of Gal1int and Gal1iso at $t = 0.39$ Gyr (using DiskFit) and of their 2D O/H maps. The results are shown in the top and middle panels of Fig. 15. For comparison purposes, we re-derive the radial velocity profile of NGC 2535 to include the region beyond the ocular by constraining all kinematic parameters to the values reported in Table 2. It is interesting to note that both Gal1int and NGC 2535 exhibit a steep decrease beyond $\sim 25''$ whereas the velocity profile of Gal1iso reaches a plateau. The decrease is not continuous but rather reflects the constant velocities over long patches in the stretched tidal tails caused by streaming motions. The same effect explains the constant values for the metallicity

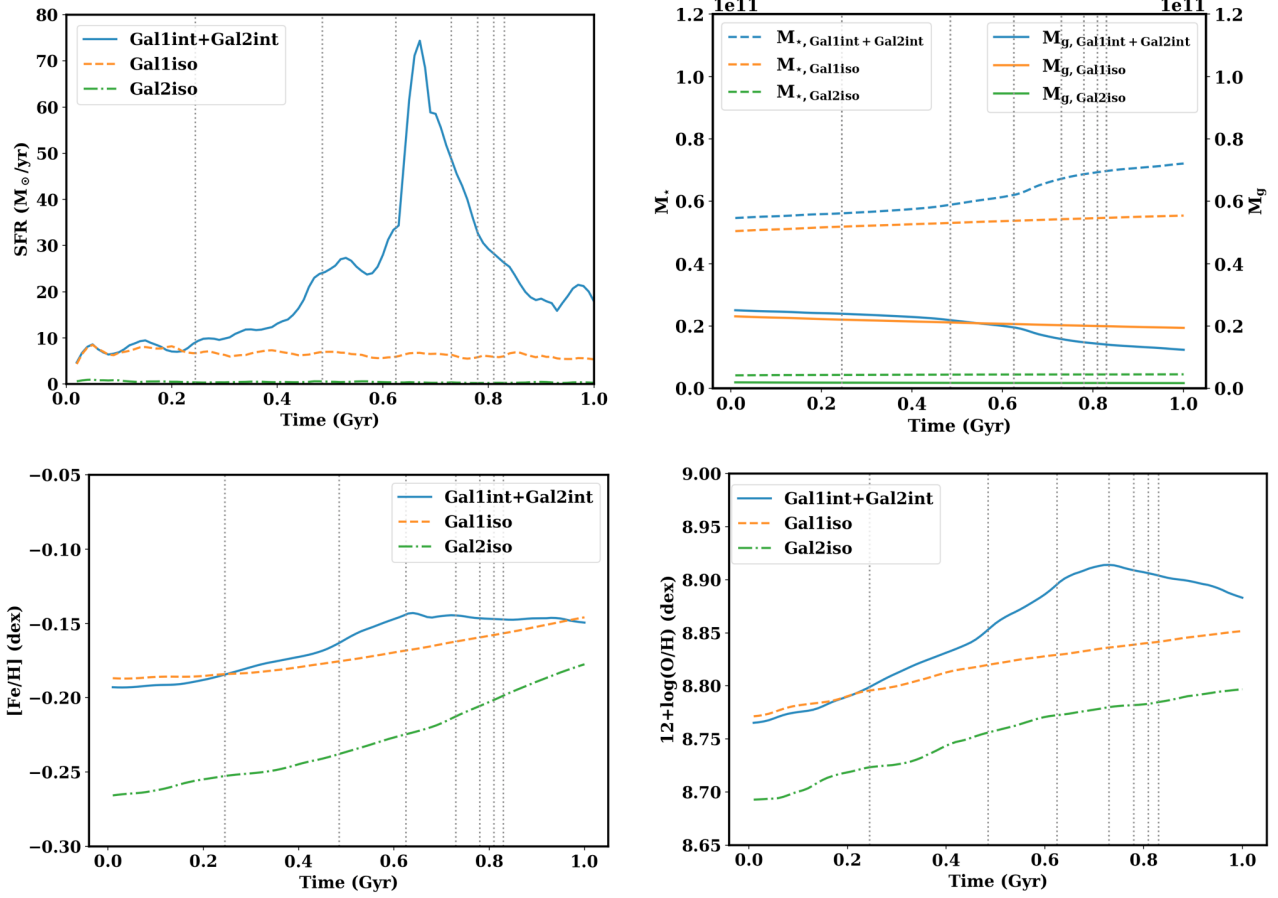


FIGURE 16. Temporal evolution of global star formation, stellar mass, gas mass, average Fe/H and O/H in Gal1int+Gal2int, Gal1iso and Gal2iso.

over long patches of the tidal tails as well. Also of interest, there is a noticeable difference between the velocity profiles of Gal1int and Gal1iso in the inner $\sim 15''$ where the amplitude is bigger in Gal1int. Earlier simulations have revealed that ocular wave in interacting galaxies results from the inflow and speed up of material in the two quadrants that lose angular momentum as a result of a quasi-impulsive encounter at closest approach (Struck 1999; Elmegreen et al. 1995, 1991). This inflow accounts for both the density increase and the centrifugal speed-up in Gal1int. The velocity profiles of Gal1int and NGC 2535 are very similar in shapes although we point out a slight difference in radial velocity values in the inner and outer parts of the ionized gas disks. From Fig. 15, Gal1int and NGC 2535 have similar oxygen abundance profiles as well, both exhibiting a break beyond the radius of $\sim 25''$ albeit with a big scatter in NGC 2535 values whereas the profile in Gal1iso could be fitted with a single slope. Inside this radius, O/H values of Gal1int are systematically lower than the values of Gal1iso although the difference is very little. Hence, the inner slopes of O/H vs. radius for Gal1int and Gal1iso would be comparable. Data points for the O/H profiles in the simulated galaxies are obtained by averaging over concentric annuli (centre, P.A. and ellipticity derived from the kinematic analysis) and error bars correspond to the standard deviation at a given radius. The data points from the observations are measured abundances of the HII region complexes detected in NGC 2535 and their corresponding uncertainties. O/H values over the entire disk of Gal2int are very close, predicting a shallow abundance profile, although the complexity and mismatch of the velocity map to that of NGC 2536 does

not allow us to carry out the same radial analysis on Gal2int. We also investigated the distribution of the iron abundance in the simulated galaxies. The corresponding profiles, shown in the bottom panel of Fig. 15, are also obtained by averaging [Fe/H] values of Gal1int and Gal1iso over concentric annuli. [Fe/H] distribution could be fitted with a single slope for Gal1iso and two slopes for Gal1int. For the interacting galaxy, the outer slope, beyond the break radius, is still shallow. Inside the break radius, [Fe/H] values for Gal1int are still systematically lower than the values for Gal1iso but the difference is more noticeable compared to the O/H values.

4.3.4 Global properties

Fig. 16 shows the time evolution of the global SFR, stellar and gaseous masses, iron and oxygen abundances. Before the first pericentre passage, the total SFR in the interacting system is almost constant at around $7.5 M_{\odot} \text{ yr}^{-1}$ and is comparable to the SFR in Gal1iso. SFR in Gal2iso is negligible. The global SFR in isolated galaxies Gal1iso and Gal2iso stays almost constant throughout the run. After the first pericentre passage ($t = 0.25$ Gyr), the global SFR in Gal1int+Gal2int increases linearly to reach $12.3 M_{\odot} \text{ yr}^{-1}$ at $t = 0.39$ Gyr, matching the value derived from observations. At this moment, the total stellar mass is $5.73 \times 10^{10} M_{\odot}$ and total gas mass is $3.22 \times 10^{10} M_{\odot}$, of which $2.3 \times 10^{10} M_{\odot}$ is hydrogen, matching the estimated masses from observations. Right before the second pericentre passage, at $t = 0.43$ Gyr, it increases significantly to be

$24 M_{\odot} \text{ yr}^{-1}$ at the second pericentre passage, at $t = 0.49$ Gyr. The global SFR is $33 M_{\odot} \text{ yr}^{-1}$ by the time Gal1int and Gal2int are at their third closest separation at $t = 0.63$ Gyr. Past the third pericentre passage, the global SFR increases drastically to reach its peak at $74 M_{\odot} \text{ yr}^{-1}$ (ten times the corresponding value in Gal1int at the same time) in only 0.04 Gyr. After this, it decreases linearly. When the galaxies have coalesced, at $t = 0.83$ Gyr, the value of the SFR of the system is comparable to that at the second pericentre passage, three times lower the value at its peak. The evolution of the stellar/gaseous masses in Gal1int+Gal2int is related to the SFR. The slope of the M_{\star}/M_{g} vs. time increase/decrease at $t = 0.25, 0.43$ and 0.63 Gyr. After $t = 0.67$ Gyr, the changes in slopes are moderate even if the gaseous mass is 70 per cent its initial value : the available gas is heated and is not used to form new stars. The masses in the isolated galaxies change very little comparatively throughout the run as the corresponding SFRs are low. The bottom panels of Fig. 16 show the temporal evolution of O/H and Fe/H averaged over the entire systems (Gal1int+Gal2int, Gal1iso, and Gal2iso). The evolution of O/H is closely related to the evolution of the global SFR. At the beginning, O/H in Gal1int+Gal2int is similar to O/H in Gal1iso. O/H rises at rates that change almost at the times, as discussed above, where the global SFR accelerates but with a small delay. The evolution of Fe/H tends to be more steady, even in the isolated galaxies. These differences can be explained by the different lifetimes of Type II and Type Ia SNe progenitors. Since oxygen is mainly produced by Type II SNe, their very short lifetimes progenitors make the histories of SF and oxygen enrichment correlated. Type Ia SNe, which mainly contribute to the production of iron, have very long lifetimes progenitors. Then, a significant fraction of iron is produced long after the SFR has reached its peak, hence the notable difference between O/H and Fe/H histories.

4.3.5 Inside the central regions

We also computed the central SFRs and metallicities to see how the evolution of these quantities compares to the global ones. Fig. 17 shows the history of the SFR, O/H and Fe/H averaged over a spherical region of radius 3 kpc centered on the centres of mass of Gal1int and Gal2int. The central SFRs increase significantly at the third pericentre passage but Gal2int exhibits a burst of central SF at the second pericentre passage. The central SFRs in Gal1int and Gal2int after the third pericentre passage account for more than half of the global SFR. We note that the central SFR in Gal1int is more sensitive to the separation between the galaxies after the third pericentre passage as it exhibits enhancements when the galaxies are at their closest passages. The central chemical evolution differs from the global one. Initially, there is a drop in O/H and Fe/H caused by low metallicity gas channeled to the centre. The effect is more noticeable for Gal2int since the companion is more affected by the tidal forces as discussed above. The production of oxygen and iron (but to a lesser extent) by Type II SNe compensates this initial drop. The metals enrichment ends up surpassing the increase in hydrogen in the centre and drives up the rise in the history of Fe/H and O/H. This rise is correlated to the bursts of SF in Gal2int and Gal1int at the second and third pericentre passages respectively. There is a change of slope in O/H at $t = 0.78$ Gyr due to the decline of central SFRs at the same time. Since iron is produced mainly by Type Ia SNe with long lifetimes progenitors, the change of slope does not happen in the history of Fe/H.

The limited resolution of the algorithm might be responsible for the high central abundances that are reached by the end of the simulation. The spike in SFR after the third pericentre passage should lead to

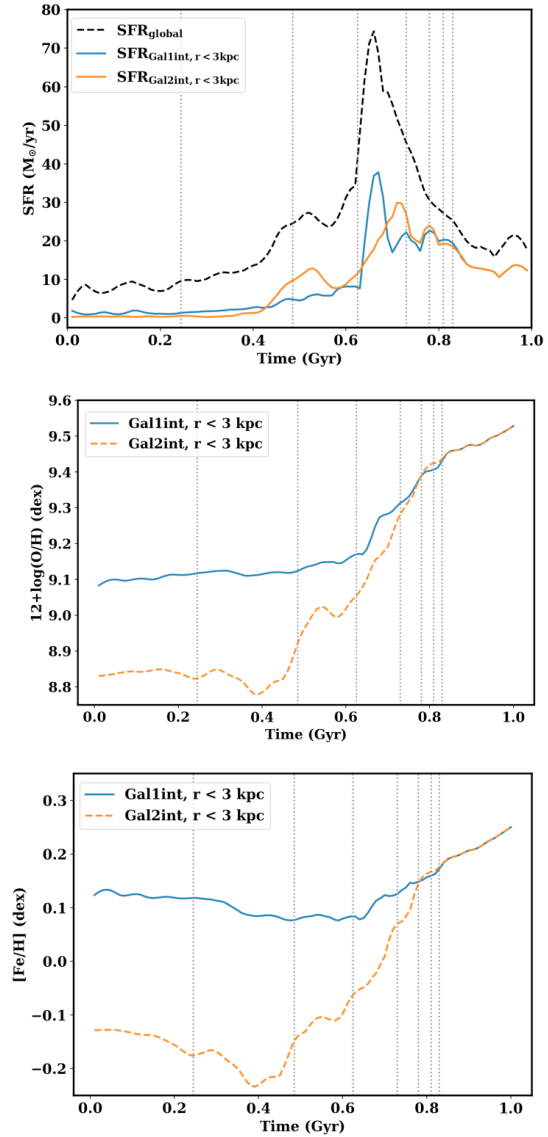


FIGURE 17. Temporal evolution of the central SFR (upper panel), iron and oxygen abundances (middle and lower panel respectively) of Gal1int and Gal2int.

significant feedback, that would regulate star formation. However, the decrease in central SFR after the spike is quite slow, suggesting that, once the central gas density reaches a certain value, the simulation underestimate the strength of feedback at the current resolution. We note that this occurs long after the present time $t = 0.39$ Gyr. Hence, this does not impact our comparison between the simulation and the observations.

4.3.6 Effect of the resolution of the numerical simulation

In the previous sections, we presented a suite of three numerical simulations : two of isolated galaxies, and one of interacting galaxies, with the goal of reproducing the observations of NGC 2535 and NGC 2536. To test the robustness of the comparison, we started a fourth simulation of interacting galaxies, using the same initial conditions but four times as many gas and dark matter particles. The purpose of this high-resolution run is to allow a comparison

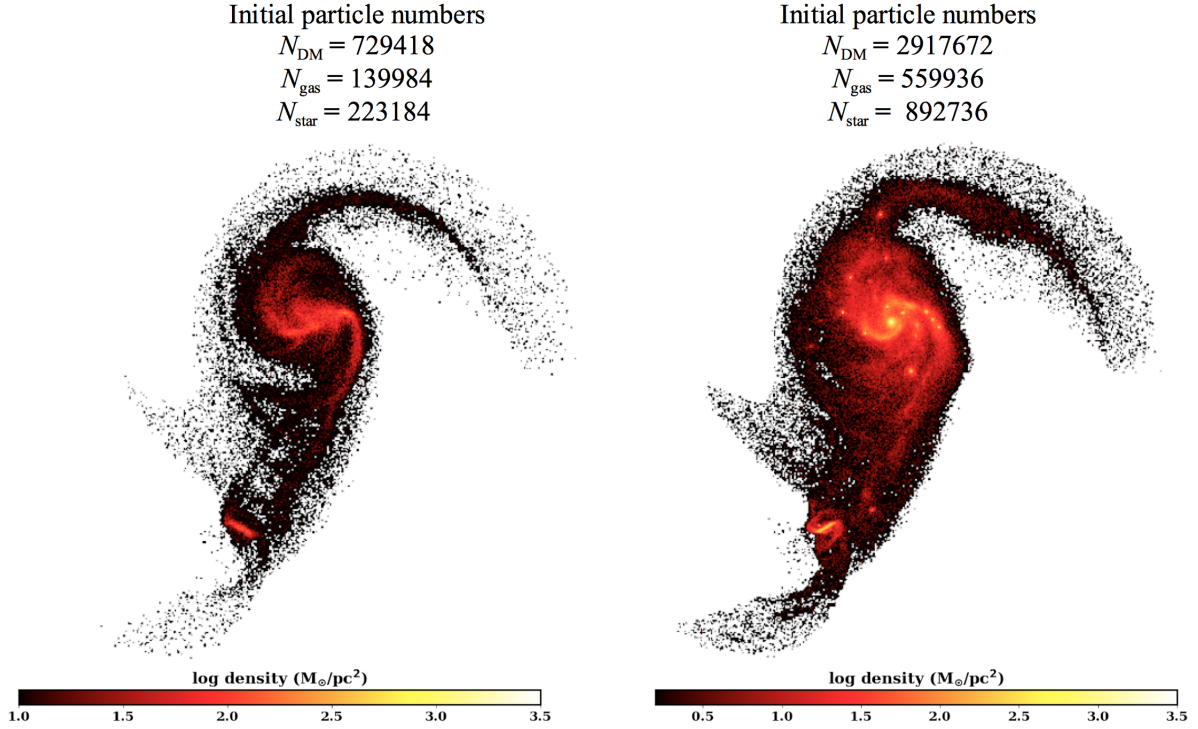


FIGURE 18. Stellar component snapshots at $t = 0.39$ Gyr in the xy plane of the simulation presented in this work (left) and a higher resolution simulation (right). Top labels refer to the initial numbers of particles in the simulations.

with the low-resolution run and the observations at the present. We are particularly interested in small morphological features that are present in the observations, but not reproduced in the low-resolution simulation. Since the computational cost was getting excessive, we did not push this new simulation beyond $t = 0.39$ Gyr.

Fig. 18 shows snapshots at $t = 0.39$ Gyr of the stellar component in the plane of the sky, for the original simulation and the higher-resolution one. The morphological structures induced by the interaction in the primary galaxy stand out more clearly in the higher resolution simulation and the satellite galaxy displays a bar and spiral arms that are more tightly wound. Furthermore, the thin dense region in the extended tidal arm on the anti-companion side is less curved and appears broken. The higher number of gas particles allows a better sampling of higher gas density regions leading to more stars being formed. This explains the condensations or clumps in the stellar components, visible in the tidal features at high resolution (yellow spots in Fig. 18).

In this first high-resolution simulation, the SFR is higher than in the low-resolution one, because we did not adjust the value of the parameter C^* in equation (4) to account for the fact that, at higher resolution, the algorithm can resolve regions with higher gas densities. We defer this to future work, as our main objective here was to assess the effect of resolution on the morphology of the system.

5 SUMMARY AND CONCLUSIONS

We presented kinematics and metallicity analysis of the interacting pair of star-forming galaxies Arp 82 using SITELLE data. We also investigated the effects of the interaction using a numerical model that reproduces some of the properties of the interacting galaxies NGC 2535 and NGC 2536. The kinematics and photometry analysis

of NGC 2536 reveal that the satellite galaxy is barred. The observed velocity map of NGC 2535 is axisymmetric inside the ocular ring with a small bump in the inner $10''$ (3 kpc). The numerical model reproduces the shape of this velocity profile. Comparison to the kinematics of the simulated primary galaxy evolved in isolation shows that the bump is induced by the interaction. An increase in central densities during the interaction drives the rise in central velocities. Beyond the eye-shaped structure of NGC 2535, at $r > 25''$ (7 kpc), we find strong streaming motions around the ocular and along the tidal tails with constant velocities over long patches in the velocity map and a corresponding strong decrease in the velocity profile of the receding side at this radius. Peculiar velocities or velocity kinks in the H α velocity map of NGC 2535 bring out another structure with an elliptical shape. This elliptical arc is also detected in SITELLE deep images. The numerical model reproduces the observed ocular, the spurs around the ocular, the elliptical arc, and tidal tails and shows that these features are induced by the interaction. It also reproduces the intrinsic ellipticity of the stellar disk of NGC 2535 induced by the interaction at the first close encounter in a direction almost perpendicular to the kinematic P.A. In fact, these features are produced after the galaxies have experienced a first collision, half way in their race to a second collision. Tidal forces at the first collision result in most of the outer gas of the satellite galaxy being pulled off, and the inner gas disk experiencing several distortions. The subsequent mixing leaves the residual inner disk with an almost uniform value of metallicity with some of the removed gas, with low metallicity, falling back on it. This could explain the very shallow oxygen abundance radial profile observed for NGC 2536. For the primary galaxy, at the best match configuration, only the outer disk is affected, with the tidal tails showing constant metallicity over long patches. This result in a break in the metallicity profile, similar to the one observed for NGC 2535.

The numerical model also reproduces the observed global SFR of Arp 82 and its total stellar/gas mass. The global SFR is about one and a half times that of the primary galaxy evolved in isolation. The corresponding central SFRs are not important, meaning that the induced SF is spatially extended. The central oxygen abundance of the satellite galaxy is lower compared to its initial value and its O/H radial profile is flattened by the interaction. However, for the primary galaxy, the central oxygen abundance does not change much from its initial value and its O/H radial profile, inside the ocular, is comparable to that of normal isolated star forming galaxies. The global SFR in the simulation reaches its peak when the two galaxies are still separated. At its peak, the global SFR is about ten times its value in the primary galaxy evolved in isolation, consistent with what is measured for bright local starbursts. When the galaxies have merged, the global SFR is three times lower compared to its peak value. The results presented in this work show that the changes induced by the interaction are a function of the interaction stage and galaxies properties. Early statistical studies investigated properties of interacting galaxies based on pair separations and relative velocity. Since the projected distances between pairs of galaxies does not really represent their physical separations and is not correlated to the interaction stage, detailed studies of specific nearby systems are crucial for a better characterization of the properties of interacting galaxies.

ACKNOWLEDGEMENTS

Based on observations obtained with SITELE, a joint project of Université Laval, ABB, Université de Montréal and the Canada-France-Hawaii Telescope (CFHT), which is operated by the National Research Council of Canada, the Institut National des Sciences de l'Univers of the Centre National de la Recherche Scientifique of France and the University of Hawaii. The authors wish to recognize and acknowledge the very significant cultural role that the summit of Mauna Kea has always had within the indigenous Hawaiian community. We are most grateful to have the opportunity to conduct observations from this mountain. LD and HM are grateful to the Natural Sciences and Engineering Research Council of Canada, the Fonds de Recherche du Québec, and the Canada Foundation for Innovation for financial support. JIP and JVM acknowledge financial support from projects Estallidos6 AYA2016-79724-C4 (Spanish Ministerio de Economía y Competitividad), Estallidos7 PID2019-107408GB-C64 (Spanish Ministerio de Ciencia e Innovación), grant P18-FR-2664 (Junta de Andalucía), and grant SEV-2017-0709 "Centro de Excelencia Severo Ochoa Program" (Spanish Science Ministry). We thank the referee, Dr. Curtis Struck, for a thorough review of this paper and valuable suggestions.

DATA AVAILABILITY STATEMENT

The data underlying this article will be shared on reasonable request to the authors.

Références

Amram P., Marcellin M., Boulesteix J., Le Coarer E., 1989, *A&AS*, **81**, 59
 Baldwin J. A., Phillips M. M., Terlevich R., 1981, *PASP*, **93**, 5
 Barrera-Ballesteros J. K., et al., 2015, *A&A*, **579**, A45
 Blumenthal K. A., Barnes J. E., 2018, *MNRAS*, **479**, 3952

Bournaud F., Duc P. A., Amram P., Combes F., Gach J. L., 2004, *A&A*, **425**, 813
 Bresolin F., 2007, *ApJ*, **656**, 186
 Buat V., Xu C., 1996, *A&A*, **306**, 61
 Calzetti D., 2001, *PASP*, **113**, 1449
 Cardelli J. A., Clayton G. C., Mathis J. S., 1989, *ApJ*, **345**, 245
 Courteau S., 1997, *AJ*, **114**, 2402
 Di Matteo P., Combes F., Melchior A. L., Semelin B., 2007, *A&A*, **468**, 61
 Drew P. M., Casey C. M., Burnham A. D., Hung C.-L., Kassim S. A., Simons R. C., Zavala J. A., 2018, *ApJ*, **869**, 58
 Drissen L., Rousseau-Nepton L., Lavoie S., Robert C., Martin T., Martin P., Mandar J., Grandmont F., 2014, *Advances in Astronomy*, **2014**, 293856
 Drissen L., et al., 2019, *MNRAS*, **485**, 3930
 Duc P.-A., 2012, *Astrophysics and Space Science Proceedings*, **28**, 305
 Elbaz D., et al., 2007, *A&A*, **468**, 33
 Ellison S. L., Mendel J. T., Patton D. R., Scudder J. M., 2013, *MNRAS*, **435**, 3627
 Elmegreen D. M., Sundin M., Elmegreen B., Sundelius B., 1991, *A&A*, **244**, 52
 Elmegreen D. M., Kaufman M., Brinks E., Elmegreen B. G., Sundin M., 1995, *ApJ*, **453**, 100
 Hancock M., Smith B. J., Struck C., Giroux M. L., Appleton P. N., Charmandaris V., Reach W. T., 2007, *AJ*, **133**, 676
 Holmbeck A. J., et al., 2016, *MNRAS*, **459**, 720
 Howard S., Keel W. C., Byrd G., Burkey J., 1993, *ApJ*, **417**, 502
 Kauffmann G., et al., 2003, *MNRAS*, **346**, 1055
 Kaufman M., Brinks E., Elmegreen D. M., Thomasson M., Elmegreen B. G., Struck C., Klaric M., 1997, *AJ*, **114**, 2323
 Kawata D., Gibson B. K., 2003, *MNRAS*, **340**, 908
 Kawata D., Okamoto T., Gibson B. K., Barnes D. J., Cen R., 2013, *MNRAS*, **428**, 1968
 Kennicutt Robert C. J., 1998, *ARA&A*, **36**, 189
 Kennicutt Robert C. J., Keel W. C., van der Hulst J. M., Hummel E., Roettiger K. A., 1987, *AJ*, **93**, 1011
 Kewley L. J., Dopita M. A., 2002, *ApJS*, **142**, 35
 Kewley L. J., Ellison S. L., 2008, *ApJ*, **681**, 1183
 Kewley L. J., Dopita M. A., Sutherland R. S., Heisler C. A., Trevena J., 2001, *ApJ*, **556**, 121
 Kewley L. J., Geller M. J., Barton E. J., 2006, *AJ*, **131**, 2004
 Kewley L. J., Rupke D., Zahid H. J., Geller M. J., Barton E. J., 2010, *ApJ*, **721**, L48
 Knapen J. H., Cisternas M., Querejeta M., 2015, *MNRAS*, **454**, 1742
 Kobulnicky H. A., Kewley L. J., 2004, *ApJ*, **617**, 240
 Kumari N., Maiolino R., Belfiore F., Curti M., 2019, *MNRAS*, **485**, 367
 Lee J. C., Hwang H. S., Lee M. G., Kim M., Lee J. H., 2012, *ApJ*, **756**, 95
 Marino R. A., et al., 2013, *A&A*, **559**, A114
 Martin T., Drissen L., Joncas G., 2015, in Taylor A. R., Rosolowsky E., eds, *Astronomical Society of the Pacific Conference Series Vol. 495, Astronomical Data Analysis Software and Systems XXIV (ADASS XXIV)*. p. 327
 Martin T. B., Prunet S., Drissen L., 2016, *MNRAS*, **463**, 4223
 Martin T. B., Drissen L., Melchior A.-L., 2018, *MNRAS*, **473**, 4130
 Martin T., Drissen L., Prunet S., 2021, *MNRAS*, **505**, 5514
 Mihos J. C., Hernquist L., 1994, *ApJ*, **425**, L13
 Murphy E. J., et al., 2011, *ApJ*, **737**, 67
 Navarro J. F., Frenk C. S., White S. D. M., 1996, *ApJ*, **462**, 563
 Osterbrock D. E., Ferland G. J., 2006, *Astrophysics of gaseous nebulae and active galactic nuclei*. University Science Books
 Pérez-Montero E., 2014, *MNRAS*, **441**, 2663
 Pérez-Montero E., García-Benito R., Hägele G. F., Díaz Á. I., 2010, *MNRAS*, **404**, 2037
 Persic M., Salucci P., 1991, *ApJ*, **368**, 60
 Pilyugin L. S., Grebel E. K., 2016, *MNRAS*, **457**, 3678
 Privon G. C., Barnes J. E., Evans A. S., Hibbard J. E., Yun M. S., Mazzarella J. M., Armus L., Surace J., 2013, *ApJ*, **771**, 120
 Renaud F., Bournaud F., Duc P.-A., 2015, *MNRAS*, **446**, 2038
 Rupke D. S. N., Kewley L. J., Barnes J. E., 2010, *ApJ*, **710**, L156
 Salpeter E. E., 1955, *ApJ*, **121**, 161

- Sánchez S. F., et al., 2014, *A&A*, **563**, A49
- Sanders D. B., Mirabel I. F., 1996, *ARA&A*, **34**, 749
- Schawinski K., Thomas D., Sarzi M., Maraston C., Kaviraj S., Joo S.-J., Yi S. K., Silk J., 2007, *MNRAS*, **382**, 1415
- Sellwood J. A., Sánchez R. Z., 2010, *MNRAS*, **404**, 1733
- Sellwood J. A., Spekkens K., 2015, arXiv e-prints, p. arXiv:1509.07120
- Spekkens K., Sellwood J. A., 2007, *ApJ*, **664**, 204
- Struck C., 1999, *Phys. Rep.*, **321**, 1
- Thilker D. A., Braun R., Walterbos R. A. M., 2000, *AJ*, **120**, 3070
- Thilker D. A., Walterbos R. A. M., Braun R., Hoopes C. G., 2002, *AJ*, **124**, 3118
- Toomre A., 1977, in Tinsley B. M., Larson R. B. Gehret D. C., eds, *Evolution of Galaxies and Stellar Populations*. p. 401
- Toomre A., Toomre J., 1972, *ApJ*, **178**, 623
- Torres-Flores S., Scarano S., Mendes de Oliveira C., de Mello D. F., Amram P., Plana H., 2014, *MNRAS*, **438**, 1894
- Weilbacher P. M., Duc P. A., Fritze-v. Alvensleben U., 2003, *A&A*, **397**, 545
- Zaragoza-Cardiel J., Smith B. J., Rosado M., Beckman J. E., Bitsakis T., Camps-Fariña A., Font J., Cox I. S., 2018, *ApJS*, **234**, 35
- Zasov A. V., Saburova A. S., Egorov O. V., Dodonov S. N., 2019, *MNRAS*, **486**, 2604
- Zibetti S., Charlot S., Rix H.-W., 2009, *MNRAS*, **400**, 1181

APPENDIX A: ADDITIONAL TABLE AND FIGURE

TABLE A1: Positions and fluxes (uncorrected for reddening) of the HII region complexes detected in Arp 82. Fluxes are in units of 10^{-16} erg s $^{-1}$ cm $^{-2}$.

Region ID	R.A	Dec	[OII] λ 3727	H β	[OIII] λ 5007	H α	[NII] λ 6583	[SII] λ 6716	[SII] λ 6731
1	8h11m17s	+25°12'29"	0.85±0.82	0.95±0.20	0.39±0.20	2.53±0.30	0.37±0.20	0.66±0.22	0.24±0.21
2	8h11m17s	+25°12'06"	2.62±0.77	1.16±0.25	2.82±0.26	4.48±0.21	0.26±0.20	0.93±0.22	0.31±0.22
3	8h11m17s	+25°10'35"	4.06±0.91	2.11±0.25	3.65±0.26	7.27±0.32	0.50±0.30	0.73±0.33	0.54±0.33
4	8h11m16s	+25°10'40"	0.82±0.50	0.67±0.16	0.67±0.16	2.09±0.16	0.05±0.16	0.35±0.17	0.43±0.17
5	8h11m16s	+25°10'42"	0.93±0.56	0.39±0.16	0.63±0.16	2.01±0.35	0.27±0.23	0.46±0.25	0.46±0.25
6	8h11m16s	+25°11'02"	3.87±1.12	2.07±0.36	4.11±0.37	6.19±0.38	0.84±0.36	1.07±0.40	0.78±0.40
7	8h11m16s	+25°10'47"	6.44±1.32	3.58±0.55	4.27±0.55	21.95±0.82	5.58±0.55	5.40±0.60	3.35±0.59
8	8h11m16s	+25°10'46"	8.10±0.89	6.53±0.34	8.32±0.35	28.53±0.70	6.31±0.46	5.77±0.50	3.40±0.49
9	8h11m16s	+25°10'32"	2.67±0.74	0.67±0.26	1.31±0.26	4.03±0.44	0.57±0.29	1.22±0.33	0.90±0.32
10	8h11m16s	+25°10'42"	24.15±1.62	17.07±0.61	17.10±0.62	66.62±1.34	17.12±0.90	14.09±0.96	9.64±0.95
11	8h11m16s	+25°10'58"	5.97±0.87	4.35±0.45	4.00±0.46	19.08±0.73	3.58±0.47	2.80±0.51	3.02±0.52
12	8h11m16s	+25°10'45"	39.83±2.42	29.75±0.98	21.68±0.99	139.36±2.76	37.01±1.86	31.79±1.99	23.64±1.98
13	8h11m16s	+25°11'25"	4.44±0.93	1.35±0.32	4.06±0.33	6.35±0.32	0.81±0.30	1.31±0.33	0.89±0.33
14	8h11m16s	+25°12'27"	1.09±0.37	0.13±0.15	0.84±0.15	1.05±0.24	0.31±0.16	0.27±0.17	0.19±0.17
15	8h11m16s	+25°10'49"	227.06±10.64	193.52±4.32	157.50±4.38	849.61±13.82	219.32±9.20	137.10±9.77	98.98±9.75
16	8h11m16s	+25°10'54"	6.97±0.95	3.41±0.36	5.70±0.37	17.35±0.64	4.55±0.42	3.46±0.45	2.58±0.45
17	8h11m16s	+25°10'44"	66.38±4.63	46.57±2.27	32.07±2.30	217.69±4.20	69.50±2.90	55.56±3.08	39.59±3.04
18	8h11m15s	+25°12'19"	4.40±0.92	1.85±0.28	1.51±0.28	6.01±0.51	0.84±0.34	1.81±0.38	1.00±0.37
19	8h11m15s	+25°10'39"	4.30±1.08	2.06±0.35	1.87±0.35	11.19±0.61	3.10±0.41	2.86±0.44	1.55±0.43
20	8h11m15s	+25°10'44"	19.29±2.05	9.70±0.97	9.35±0.98	52.97±1.32	16.58±0.90	12.64±0.96	10.41±0.95
21	8h11m15s	+25°10'49"	7.03±0.95	2.16±0.47	2.92±0.47	19.58±0.74	6.28±0.51	4.81±0.54	4.09±0.54
22	8h11m15s	+25°12'17"	5.95±1.29	3.80±0.39	4.84±0.40	14.08±0.45	3.47±0.43	2.59±0.47	2.36±0.48
23	8h11m15s	+25°12'34"	0.15±0.48	0.70±0.18	0.06±0.19	1.71±0.26	0.24±0.17	0.45±0.19	0.23±0.19
24	8h11m15s	+25°10'53"	3.61±0.81	2.15±0.41	6.78±0.42	9.65±0.51	0.92±0.33	1.66±0.36	1.47±0.36
25	8h11m15s	+25°10'47"	23.89±2.69	11.66±1.44	12.27±1.46	76.11±2.28	24.18±1.57	18.81±1.66	14.18±1.65
26	8h11m15s	+25°11'21"	0.78±0.51	0.59±0.17	0.49±0.18	2.27±0.19	0.21±0.18	0.07±0.20	0.24±0.20
27	8h11m15s	+25°12'14"	2.44±1.04	2.25±0.32	0.96±0.33	6.11±0.53	1.40±0.36	2.61±0.41	0.94±0.39
28	8h11m15s	+25°12'37"	23.94±2.60	25.06±1.05	12.36±1.06	105.53±2.20	31.05±1.50	23.15±1.59	14.57±1.58
29	8h11m15s	+25°10'38"	5.73±0.96	3.44±0.38	3.31±0.38	17.94±0.66	4.16±0.43	2.01±0.46	2.07±0.46
30	8h11m15s	+25°11'08"	2.54±1.01	2.03±0.32	2.34±0.33	6.32±0.29	1.06±0.28	0.72±0.31	0.46±0.31
31	8h11m15s	+25°12'33"	5.76±1.17	3.26±0.41	2.56±0.41	20.38±0.68	7.11±0.47	5.12±0.49	2.75±0.49
32	8h11m15s	+25°11'22"	0.53±0.51	0.27±0.12	0.29±0.12	1.05±0.14	0.28±0.13	0.17±0.14	0.17±0.14
33	8h11m15s	+25°12'45"	47.54±3.80	33.74±1.33	44.92±1.34	147.09±3.02	35.75±2.01	30.49±2.17	21.21±2.16
34	8h11m15s	+25°12'40"	8.84±1.30	6.47±0.41	5.63±0.41	34.36±0.80	9.76±0.54	7.94±0.58	5.08±0.57
35	8h11m15s	+25°10'42"	27.78±2.60	23.81±1.00	16.32±1.02	115.61±2.06	28.90±1.37	23.59±1.47	16.73±1.46
36	8h11m15s	+25°12'50"	73.97±4.50	58.12±1.56	53.88±1.58	271.65±4.41	66.57±2.94	52.35±3.16	34.85±3.14
37	8h11m15s	+25°12'28"	160.22±7.61	148.85±3.43	81.74±3.47	710.13±12.64	213.33±8.61	141.99±9.09	96.33±9.04
38	8h11m15s	+25°11'11"	6.96±1.14	4.30±0.40	6.50±0.41	15.23±0.66	2.60±0.42	2.53±0.46	1.02±0.46
39	8h11m15s	+25°10'41"	12.09±1.79	7.36±0.50	6.87±0.51	41.25±1.15	10.37±0.76	9.36±0.83	6.26±0.82
40	8h11m15s	+25°12'55"	19.45±1.84	16.64±0.69	14.08±0.70	72.31±1.46	16.58±0.96	11.84±1.04	9.82±1.04
41	8h11m14s	+25°12'19"	219.75±9.47	206.28±4.04	157.01±4.09	917.89±15.75	251.82±10.56	155.91±11.19	104.73±11.16
42	8h11m14s	+25°12'38"	3.61±1.22	4.08±0.46	1.71±0.47	19.93±0.82	7.11±0.58	5.15±0.61	2.38±0.59
43	8h11m14s	+25°10'36"	1.00±0.60	0.41±0.23	0.52±0.23	2.80±0.40	0.55±0.26	0.44±0.28	0.55±0.29
44	8h11m14s	+25°10'55"	1.74±0.55	0.22±0.20	1.33±0.20	1.34±0.16	0.02±0.16	0.42±0.17	0.73±0.17
45	8h11m14s	+25°12'41"	3.27±1.04	3.64±0.40	2.21±0.41	14.99±0.59	4.11±0.40	2.81±0.42	2.38±0.42
46	8h11m14s	+25°12'00"	1.35±0.79	0.40±0.23	0.62±0.24	3.61±0.28	0.73±0.27	0.95±0.29	0.28±0.30
47	8h11m14s	+25°12'43"	9.00±1.67	5.49±0.72	4.72±0.73	33.50±1.12	10.88±0.77	8.59±0.82	6.68±0.82
48	8h11m14s	+25°12'13"	4.58±0.99	4.20±0.32	2.63±0.32	15.17±0.55	4.26±0.37	4.48±0.41	2.93±0.40
49	8h11m14s	+25°13'00"	5.11±1.50	1.75±0.41	0.53±0.41	9.96±0.71	1.79±0.47	3.06±0.52	1.35±0.51
50	8h11m14s	+25°11'00"	0.72±0.56	0.38±0.17	0.13±0.17	1.35±0.28	0.22±0.19	0.53±0.22	0.30±0.21
51	8h11m14s	+25°13'02"	1.12±0.57	0.63±0.21	0.81±0.21	3.07±0.21	0.54±0.20	0.11±0.22	0.42±0.22
52	8h11m14s	+25°12'18"	6.31±1.12	8.04±0.56	2.03±0.57	33.45±0.99	11.71±0.69	6.50±0.71	4.16±0.71
53	8h11m14s	+25°12'27"	3.36±1.82	6.42±0.70	2.21±0.71	31.38±1.31	10.04±0.90	5.77±0.94	5.86±0.95
54	8h11m14s	+25°12'21"	2.56±1.33	1.63±0.53	0.02±0.53	10.30±0.51	3.42±0.48	2.80±0.53	0.89±0.54

...

Table A1 : Cont.

Region ID	R.A	Dec	[OII] λ 3727	H β	[OIII] λ 5007	H α	[NII] λ 6583	[SII] λ 6716	[SII] λ 6731
55	8h11m14s	+25°12'12"	56.28±3.85	43.88±1.39	39.68±1.41	168.37±3.26	45.07±2.19	36.14±2.34	22.97±2.32
56	8h11m14s	+25°11'05"	6.15±1.86	3.23±0.43	7.82±0.44	14.43±0.77	1.47±0.49	2.53±0.55	2.06±0.54
57	8h11m14s	+25°12'39"	4.61±1.43	2.14±0.52	1.43±0.52	11.29±0.69	4.10±0.48	2.54±0.50	2.41±0.50
58	8h11m14s	+25°12'28"	1.81±1.12	1.27±0.45	0.31±0.45	4.38±0.41	1.88±0.39	1.07±0.43	1.06±0.43
59	8h11m14s	+25°12'58"	0.69±0.59	0.81±0.20	0.79±0.20	2.38±0.20	0.31±0.19	0.60±0.21	0.45±0.21
60	8h11m14s	+25°13'06"	38.02±2.23	26.73±0.96	48.28±0.97	98.32±1.79	15.57±1.17	17.73±1.28	10.29±1.27
61	8h11m14s	+25°12'03"	20.88±2.30	15.13±0.77	12.65±0.78	53.66±1.07	13.75±1.02	12.30±1.12	6.30±1.13
62	8h11m14s	+25°11'11"	1.27±0.65	0.59±0.22	1.02±0.23	3.08±0.29	0.64±0.19	0.61±0.20	0.14±0.20
63	8h11m14s	+25°12'45"	24.13±2.67	16.32±0.94	10.10±0.96	75.30±1.58	21.56±1.06	14.85±1.13	11.43±1.13
64	8h11m14s	+25°12'25"	1.69±0.80	0.73±0.40	0.73±0.40	4.59±0.33	1.69±0.32	1.62±0.35	0.58±0.35
65	8h11m14s	+25°11'14"	26.49±1.97	19.46±0.94	46.96±0.95	77.23±1.38	11.02±0.89	10.54±0.97	7.72±0.97
66	8h11m14s	+25°11'37"	0.21±0.60	0.20±0.18	0.37±0.18	1.29±0.29	0.27±0.19	0.24±0.21	0.25±0.21
67	8h11m14s	+25°12'03"	2.36±0.77	1.32±0.24	0.66±0.24	6.08±0.27	1.63±0.25	1.25±0.28	0.94±0.28
68	8h11m14s	+25°12'30"	1.98±0.85	0.53±0.40	0.34±0.40	4.98±0.37	2.45±0.35	1.33±0.38	1.13±0.39
69	8h11m14s	+25°13'09"	190.39±8.09	154.10±5.24	419.99±5.30	632.79±10.38	84.14±6.69	67.19±7.27	47.69±7.28
70	8h11m14s	+25°12'48"	1.32±0.54	1.01±0.19	0.97±0.19	4.21±0.20	1.18±0.19	0.66±0.21	0.62±0.21
71	8h11m13s	+25°12'11"	50.04±4.02	56.22±1.91	20.24±1.94	226.10±4.88	69.23±3.32	45.16±3.50	24.98±3.47
72	8h11m13s	+25°12'44"	0.94±0.58	1.32±0.22	0.37±0.22	3.39±0.35	1.17±0.25	1.41±0.28	1.06±0.27
73	8h11m13s	+25°11'17"	1.31±0.52	0.40±0.21	0.54±0.22	2.56±0.35	0.62±0.23	0.82±0.26	0.16±0.25
74	8h11m13s	+25°13'11"	4.66±0.61	3.45±0.23	6.20±0.24	13.42±0.44	2.03±0.29	2.09±0.31	1.24±0.31
75	8h11m13s	+25°12'27"	0.64±0.61	0.24±0.31	0.40±0.31	2.45±0.34	1.28±0.32	0.98±0.35	0.03±0.35
76	8h11m13s	+25°11'13"	2.19±0.90	1.46±0.25	2.17±0.25	6.20±0.41	1.00±0.27	1.39±0.30	0.61±0.29
77	8h11m13s	+25°12'33"	16.60±3.09	21.07±1.28	6.24±1.30	92.36±2.41	30.30±1.65	16.97±1.72	9.86±1.71
78	8h11m13s	+25°12'46"	3.27±1.01	1.89±0.37	2.00±0.37	8.69±0.41	3.00±0.39	2.13±0.43	1.50±0.43
79	8h11m13s	+25°13'12"	7.54±0.94	4.35±0.37	8.35±0.37	17.82±0.59	3.23±0.38	2.64±0.42	1.47±0.42
80	8h11m13s	+25°11'33"	0.81±0.67	0.46±0.24	0.97±0.24	2.27±0.31	0.97±0.23	0.47±0.23	0.44±0.23
81	8h11m13s	+25°13'07"	0.65±0.44	0.83±0.16	1.09±0.16	2.16±0.26	0.51±0.17	0.48±0.19	0.38±0.18
82	8h11m13s	+25°11'38"	3.46±0.97	2.04±0.30	1.01±0.30	7.02±0.60	2.70±0.43	1.85±0.45	2.04±0.45
83	8h11m13s	+25°12'25"	32.33±5.20	89.28±4.15	15.23±4.20	557.20±12.08	225.93±8.61	75.84±8.60	59.13±8.60
84	8h11m13s	+25°12'39"	2.20±1.05	0.96±0.49	1.34±0.49	5.08±0.68	2.65±0.52	1.72±0.52	0.61±0.51
85	8h11m13s	+25°12'03"	1.88±0.81	0.75±0.36	0.93±0.37	3.69±0.32	1.05±0.30	1.08±0.34	1.05±0.34
86	8h11m13s	+25°12'45"	3.83±0.94	2.22±0.38	2.63±0.39	11.19±0.61	3.65±0.42	3.03±0.45	2.91±0.45
87	8h11m13s	+25°11'24"	12.91±1.90	6.32±0.80	8.38±0.82	29.27±1.16	8.13±0.78	6.80±0.84	4.29±0.83
88	8h11m13s	+25°12'33"	1.11±0.68	0.08±0.29	0.69±0.30	4.05±0.46	1.81±0.33	0.17±0.32	0.22±0.32
89	8h11m13s	+25°12'42"	1.92±0.46	1.52±0.24	0.39±0.24	4.17±0.25	1.77±0.24	1.22±0.26	0.71±0.26
90	8h11m13s	+25°13'04"	1.43±0.54	0.31±0.23	0.82±0.24	2.62±0.35	0.38±0.23	0.49±0.25	0.41±0.25
91	8h11m13s	+25°11'43"	2.70±0.78	1.07±0.28	0.22±0.29	5.09±0.50	1.86±0.35	1.09±0.37	0.55±0.36
92	8h11m13s	+25°12'10"	3.77±1.32	1.71±0.55	1.74±0.56	12.36±0.98	4.06±0.67	3.37±0.72	1.11±0.70
93	8h11m13s	+25°12'15"	3.60±1.96	3.95±1.37	2.41±1.38	12.55±1.77	3.80±1.21	2.64±1.29	2.90±1.30
94	8h11m13s	+25°12'33"	2.95±1.32	1.58±0.54	0.32±0.55	10.82±0.78	4.08±0.55	3.65±0.59	0.86±0.57
95	8h11m13s	+25°11'21"	28.35±2.29	17.82±0.93	23.76±0.94	60.28±1.57	12.55±1.03	14.08±1.13	9.80±1.12
96	8h11m13s	+25°12'13"	4.65±1.32	1.01±0.64	0.12±0.65	9.40±0.49	3.57±0.47	3.04±0.51	1.96±0.52
97	8h11m13s	+25°12'25"	5.31±1.84	3.93±0.82	0.87±0.83	23.42±1.22	8.30±0.84	4.07±0.87	3.46±0.87
98	8h11m13s	+25°11'27"	30.09±2.79	18.92±1.11	21.08±1.12	72.42±1.82	15.16±1.20	16.83±1.31	11.94±1.30
99	8h11m12s	+25°13'05"	19.65±1.79	8.92±0.57	15.03±0.57	34.79±0.93	4.18±0.60	4.96±0.66	4.90±0.66
100	8h11m12s	+25°11'31"	2.60±0.81	1.98±0.27	2.10±0.27	6.95±0.44	2.22±0.30	1.72±0.32	1.65±0.32
101	8h11m12s	+25°12'38"	23.88±2.30	14.92±0.87	17.10±0.88	66.13±1.68	18.21±1.13	14.04±1.21	10.37±1.21
102	8h11m12s	+25°12'41"	3.87±0.67	2.23±0.22	1.48±0.22	10.00±0.45	2.51±0.30	2.10±0.32	1.52±0.32
103	8h11m12s	+25°12'35"	18.30±2.01	13.61±0.65	6.93±0.66	60.43±1.49	20.20±1.03	12.19±1.07	8.51±1.07
104	8h11m12s	+25°12'15"	3.11±1.07	1.87±0.46	0.56±0.46	9.42±0.93	4.35±0.68	2.15±0.68	1.75±0.68
105	8h11m12s	+25°12'08"	38.11±3.56	38.74±1.32	20.43±1.33	150.90±3.20	43.08±2.16	28.97±2.29	19.53±2.28
106	8h11m12s	+25°11'34"	16.11±1.83	10.64±0.57	10.55±0.58	38.04±1.21	8.39±0.80	9.75±0.88	6.42±0.87
107	8h11m12s	+25°12'33"	18.58±2.54	14.39±1.00	7.13±1.02	72.49±2.02	27.35±1.43	16.80±1.47	10.78±1.46
108	8h11m12s	+25°11'37"	13.05±1.78	8.38±0.56	7.99±0.57	35.60±0.97	8.34±0.65	8.83±0.70	6.24±0.70
109	8h11m12s	+25°12'19"	0.86±0.65	0.25±0.32	0.52±0.33	4.27±0.30	1.36±0.29	0.59±0.31	0.41±0.32
110	8h11m12s	+25°12'17"	1.31±0.69	0.18±0.31	0.25±0.31	4.50±0.46	1.45±0.31	0.53±0.32	0.22±0.32
111	8h11m12s	+25°12'21"	1.01±0.87	1.20±0.39	1.01±0.40	7.26±0.64	3.12±0.47	0.47±0.46	1.19±0.47

...

Table A1 : Cont.

Region ID	R.A	Dec	[OII] λ 3727	H β	[OIII] λ 5007	H α	[NII] λ 6583	[SII] λ 6716	[SII] λ 6731
112	8h11m12s	+25°11'40"	26.17±2.56	16.21±0.99	17.88±1.00	76.04±1.90	18.77±1.27	20.14±1.39	12.95±1.37
113	8h11m12s	+25°11'48"	1.06±0.40	0.57±0.18	0.31±0.19	1.31±0.18	0.31±0.18	0.36±0.19	0.10±0.19
114	8h11m12s	+25°12'33"	12.24±1.82	6.25±0.79	6.44±0.80	33.06±1.25	9.01±0.84	8.45±0.91	6.61±0.90
115	8h11m12s	+25°11'27"	4.41±1.75	3.55±0.47	3.96±0.47	11.92±0.83	1.60±0.55	2.82±0.61	2.11±0.60
116	8h11m12s	+25°12'16"	10.01±2.43	9.95±0.94	3.92±0.96	46.25±1.69	14.95±1.16	7.90±1.20	4.59±1.20
117	8h11m12s	+25°13'01"	2.54±0.86	1.78±0.31	1.85±0.32	6.23±0.35	1.17±0.33	1.43±0.37	1.06±0.37
118	8h11m12s	+25°12'25"	146.59±6.80	165.40±3.27	73.34±3.31	703.78±12.84	218.57±8.76	118.42±9.16	81.45±9.13
119	8h11m12s	+25°11'45"	5.30±1.28	1.49±0.40	2.35±0.40	12.32±0.63	3.07±0.42	3.72±0.47	2.46±0.46
120	8h11m12s	+25°12'06"	6.71±1.21	5.44±0.52	2.75±0.53	24.17±0.98	8.14±0.68	6.49±0.72	3.78±0.71
121	8h11m12s	+25°12'13"	19.18±2.28	14.67±0.80	9.61±0.81	73.88±1.73	21.78±1.17	14.81±1.24	11.37±1.23
122	8h11m12s	+25°11'53"	1.26±0.50	0.71±0.15	1.22±0.16	3.24±0.33	0.83±0.22	0.77±0.24	0.76±0.24
123	8h11m12s	+25°12'08"	6.02±1.38	3.10±0.65	1.67±0.66	17.24±1.11	5.49±0.76	4.11±0.81	3.69±0.81
124	8h11m12s	+25°12'19"	16.05±2.29	14.09±0.83	8.01±0.84	74.23±1.78	21.47±1.20	14.76±1.28	10.56±1.27
125	8h11m12s	+25°11'49"	1.58±0.50	0.68±0.23	0.42±0.23	3.37±0.36	0.43±0.24	1.23±0.27	0.56±0.26
126	8h11m11s	+25°12'11"	3.98±0.94	2.64±0.36	1.42±0.36	15.54±0.65	5.49±0.46	4.88±0.49	3.55±0.49
127	8h11m11s	+25°11'55"	0.88±0.75	1.08±0.19	0.81±0.19	4.49±0.31	1.15±0.21	0.75±0.22	0.75±0.22
128	8h11m11s	+25°11'57"	4.91±2.02	2.01±0.72	2.55±0.73	22.33±1.23	7.12±0.85	7.12±0.92	4.26±0.90
129	8h11m11s	+25°12'26"	2.93±1.13	0.91±0.40	2.05±0.41	6.60±0.38	1.10±0.36	0.83±0.40	0.60±0.40
130	8h11m11s	+25°12'01"	5.17±1.38	3.09±0.62	2.37±0.63	15.41±0.87	4.36±0.60	4.68±0.65	3.07±0.64
131	8h11m11s	+25°11'51"	12.02±1.37	6.48±0.63	8.18±0.64	25.83±1.09	4.92±0.72	6.27±0.79	4.03±0.78
132	8h11m11s	+25°12'36"	1.21±0.65	0.54±0.20	1.78±0.20	3.61±0.31	0.13±0.20	0.78±0.22	0.45±0.22
133	8h11m11s	+25°11'53"	1.23±0.45	0.21±0.16	0.52±0.16	1.70±0.29	0.16±0.19	0.29±0.21	0.22±0.21
134	8h11m11s	+25°12'03"	6.04±1.27	1.89±0.48	2.42±0.49	9.98±0.49	2.06±0.46	3.43±0.51	1.82±0.51
135	8h11m11s	+25°12'27"	2.99±0.86	1.72±0.24	2.02±0.24	7.52±0.44	1.61±0.29	0.65±0.31	0.49±0.31
136	8h11m11s	+25°11'58"	2.76±0.86	1.20±0.36	1.60±0.37	7.29±0.59	1.33±0.38	1.35±0.42	0.34±0.41
137	8h11m11s	+25°12'07"	2.70±0.94	1.38±0.38	1.56±0.38	5.86±0.56	1.64±0.37	0.72±0.40	1.56±0.41
138	8h11m11s	+25°13'32"	0.69±0.53	0.65±0.18	0.36±0.18	1.36±0.31	0.09±0.20	0.18±0.22	0.17±0.22
139	8h11m11s	+25°12'23"	1.69±0.77	0.42±0.23	1.11±0.23	2.82±0.28	0.21±0.18	0.50±0.20	0.52±0.20
140	8h11m10s	+25°13'36"	1.30±0.58	0.71±0.19	0.53±0.19	2.11±0.19	0.24±0.18	0.27±0.20	0.14±0.20
141	8h11m08s	+25°13'49"	1.76±0.63	0.04±0.20	0.81±0.20	2.13±0.30	0.39±0.20	0.42±0.22	0.18±0.21
142	8h11m07s	+25°13'42"	13.91±1.79	9.07±0.70	11.24±0.70	24.62±1.05	2.67±0.68	4.68±0.75	3.81±0.75
143	8h11m07s	+25°13'40"	1.38±0.64	0.51±0.20	0.67±0.21	2.04±0.18	0.15±0.18	0.21±0.19	0.15±0.19
144	8h11m06s	+25°13'38"	0.93±0.39	0.37±0.16	0.11±0.16	1.03±0.16	0.35±0.15	0.31±0.16	0.26±0.16
145	8h11m06s	+25°13'43"	1.00±0.50	0.32±0.20	0.83±0.20	1.96±0.33	0.08±0.22	0.34±0.24	0.33±0.24
146	8h11m06s	+25°13'48"	1.60±0.58	0.24±0.17	1.21±0.18	1.45±0.16	0.11±0.15	0.22±0.17	0.26±0.17
147	8h11m06s	+25°13'34"	1.50±0.61	0.60±0.19	2.69±0.19	3.21±0.30	0.36±0.19	0.30±0.21	0.64±0.21
148	8h11m05s	+25°13'32"	0.91±0.58	0.37±0.23	0.75±0.23	2.47±0.37	0.28±0.24	0.13±0.26	0.23±0.26
149	8h11m05s	+25°13'32"	5.72±1.18	3.03±0.35	4.19±0.36	9.16±0.59	1.30±0.38	1.84±0.42	1.36±0.42
150	8h11m05s	+25°13'32"	8.65±1.25	4.02±0.47	7.95±0.47	13.67±0.77	1.50±0.50	3.33±0.56	2.15±0.55
151	8h11m04s	+25°13'22"	20.82±2.04	12.89±0.68	33.21±0.69	43.40±0.96	5.20±0.62	7.93±0.69	4.06±0.68
152	8h11m03s	+25°13'04"	1.64±0.64	0.65±0.20	2.18±0.21	3.58±0.40	0.13±0.25	0.34±0.28	0.14±0.28
153	8h11m03s	+25°13'11"	0.32±0.47	0.29±0.13	0.30±0.14	1.00±0.14	0.04±0.13	0.20±0.15	0.35±0.15
154	8h11m02s	+25°13'07"	1.42±0.38	0.73±0.15	1.43±0.16	1.38±0.24	0.01±0.16	0.35±0.18	0.20±0.18
155	8h11m02s	+25°13'04"	3.17±0.81	0.81±0.27	1.02±0.27	3.36±0.22	0.31±0.21	0.70±0.23	0.57±0.23

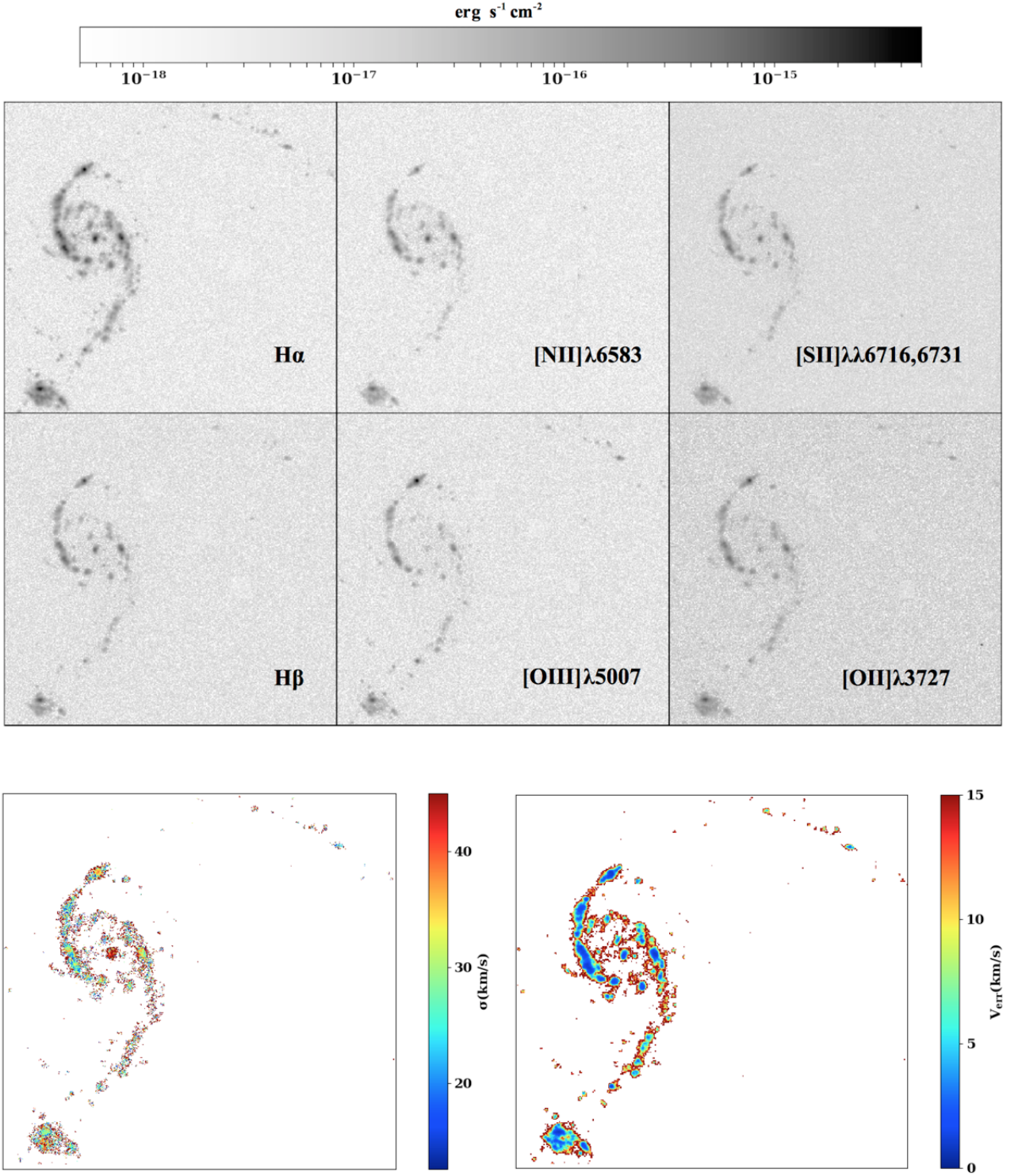


FIGURE A1. Top : Flux maps of spectral lines extracted from data cubes. Bottom : Velocity dispersion and velocity uncertainty maps; only pixels with $H\alpha$ fluxes $> 2 \times 10^{-17} \text{erg s}^{-1} \text{cm}^{-2}$, SNR > 3 and measured velocity uncertainties $< 20 \text{ km s}^{-1}$ are displayed.

This paper has been typeset from a \LaTeX file prepared by the author.